Magnetic Resonance Imaging 57 (2019) 50–67

Contents lists available at ScienceDirect

Magnetic Resonance Imaging

journal homepage: www.elsevier.com/locate/mri

Original contribution

Split Bregman method based level set formulations for segmentation and correction with application to MR images and color images

Yunyun Yang[a,*], Dongcai Tian[a], Wenjing Jia[a], Xiu Shu[a], Boying Wu[b]

[a] School of Science, Harbin Institute of Technology, Shenzhen, China
[b] School of Science, Harbin Institute of Technology, Harbin, China

ARTICLE INFO

Keywords:
Image segmentation
Intensity inhomogeneity
Split Bregman method
Bias correction
Color images
MR images

ABSTRACT

At present, magnetic resonance (MR) images have gradually become a major aid for clinical medicine, which has greatly improved the doctor's diagnosis rate. Accurate and fast segmentation of MR images plays an extremely important role in medical research. However, due to the influence of external factors and the defects of imaging devices, the MR images have severe intensity inhomogeneity, which poses a great challenge to accurately segment MR images. To deal with this problem, this paper presents an improved active contour model by combining the level set evolution model (LSE) and the split Bregman method, and gives the two-phase, the multi-phase and the vector-valued formulations of our model, respectively. The use of the split Bregman method accelerates the minimization process of our model by reducing the computation time and iterative times. A slowly varying bias field is added into the energy functional, which is the key to correct inhomogeneous images. By estimating the bias fields, not only can we get accurate image segmentation results, but also a homogeneous image after correction is provided. Then we apply our model to segment a large amount of synthetic and real MR images, including gray and color images. Experimental results show that our model can provide satisfactory segmentation and correction results for both gray and color images. Besides, compared with the LSE model, our model has higher accuracy and is superior to the LSE model. In addition, experimental results also demonstrate that our model has the advantages of being insensitive to initial contours and robust to noises.

1. Introduction

Image segmentation is a basic task and key step in image processing. To segment the part of the image that people are interested in by some certain means is the main purpose of image segmentation, which further provides effective and reliable foundation for subsequent image recognition, analysis and other processes. At present, image segmentation is mainly applied in fields such as machine vision, face recognition, traffic control systems, satellite images, pedestrian detection, medical images, and so on. In this paper, we mainly focus on the application of medical image segmentation, especially MR images segmentation, to conduct in-depth research and analysis.

In recent years, magnetic resonance imaging technology has developed rapidly and has important applications in clinical diagnosis and treatment. Due to the defects of imaging equipment and technology, MR images possess the characteristic of intensity inhomogeneity, that is, the intensity of the same tissue in MR images varies with the difference of the position. Because of this problem, the traditional image segmentation models [1-6] may incorrectly classify different issues in MR images and thus cannot accurately segment MR images.

Normally, the characteristic of intensity inhomogeneity is considered to be caused by a slowly changing bias field. In order to eliminate the adverse effect of the bias field on image segmentation, we need to estimate and correct the bias field information in the image. The existing methods of bias correction for MR images are mainly divided into two categories: prospective methods [7-10] and retrospective methods [11-14]. Both methods are to estimate the bias field in the image and divide the original image by the bias field to get the homogeneous image. For practical applications, the prospective method [10] only deals with the bias field generated by the environment equipment, but it cannot correct the inhomogeneity problem caused by the patient, which greatly limits the utilities of the prospective method in clinical medicine. However, the retrospective method [13] is applicable to most medical images because it corrects the image based on the data information carried by it. Moreover, one of the most widely used bias correction methods in the retrospective methods is based on the image segmentation [15]. Accurate segmentation results make it easier to correct the bias field. Li et al. [16] introduced a slowly varying

---

[*] Corresponding author at: G417, HIT Campus of Shenzhen University Town, Xili, Shenzhen 518055, China.
E-mail addresses: yangyunyun@hit.edu.cn, yangyunyun1986@gmail.com (Y. Yang).

https://doi.org/10.1016/j.mri.2018.10.005
Received 23 June 2018; Received in revised form 28 September 2018; Accepted 6 October 2018

bias fields and used the local intensity clustering property to propose a new active contour model that can simultaneously segment and correct the image with intensity inhomogeneity. In addition, based on the image decomposition of MR images, Li et al. [11] represented the bias field as a linear combination of 20 basis functions to propose the multiplicative intrinsic component optimization (MICO) model. Ivanovska et al. [17] introduced the smooth term of the bias field and combined with the data term and the length term to propose a novel image segmentation and correction model, in which the split Bregman method is applied to efficiently solve the minimization problems of the bias field and the level set function. Chen et al. [18] used the traditional Gaussian distribution to describe the local intensity variations, and proposed an automatic image segmentation and correction model. The homogeneous image after the bias correction makes the feature in the image more obvious and clear, which can help the doctor to improve the efficiency and accuracy of diagnosing the disease as much as possible.

Partial differential equations (PDE) and the steepest descent method are the common methods used in the image segmentation models [5,6,19-22]. However, these methods require repeated iterative calculations to solve the energy functional, which are computationally expensive and inefficient. As a result, it is an important issue to find a fast and stable numerical method for image segmentation models. In recent years, the split Bregman method [23,24] with high efficient property has been widely used in image segmentation models. Yang et al. successively applied the split Bregman method into the region scalable fitting (RSF) model [25], the improved local and global intensity fitting (ILGIF) model [26,27] and the multiphase Vese-Chan model [28]. Compared with the steepest descent method, the split Bregman method has higher computational efficiency since it greatly reduces calculation time and iterative times.

As computer technology matures, people are paying more attention to the segmentation of color images. Compared with gray images, color images can provide more plentiful and specific information, but the difficulty of segmenting them is also relatively large. Naturally, the color image segmentation is regarded as an extension of gray image segmentation to color images. Chan and Vese [29] extended their scalar Chan-Vese model [5] to the vector-valued case for color images with two-phase. Yang et al. [30] further improved the multiple Vese-Chan model for color images by defining a new energy and applying the split Bregman method to minimize the energy functional. In recent years, more and more medical color images have been used for disease diagnosis, which may become a development trend in the future. Medical color image segmentation not only is the basis of human tissue feature extraction, registration, fusion and 3D reconstruction, but also is the basis of image diagnosis. Consequently, it is essential to study the segmentation method for medical color images.

In this paper, we combine the LSE model and the split Bregman method to propose a fast image segmentation model in a variational level set formulation. We first give the two-phase level set formulation for our model and then naturally extend it to the multi-phase formulation and the vector-valued formulation. Since the energy functional of our model has the same special structure as the L1 regularization problem, so we prefer to apply the split Bregman method to minimize it efficiently, which greatly improves the speed of calculation. Large amounts of synthetic and real images with intensity inhomogeneity are used to test our model. Experimental results demonstrate that our model can succeed in segmenting inhomogeneous images, whether gray images or color images, and can provide satisfactory correction results simultaneously. Moreover, our model has the advantage of being insensitive to initial contours and robust to noise. In addition, numerical results further show that our model is superior to the LSE model.

The rest of the paper are arranged as follows. We firstly give a brief introduction for the LSE model and the split Bregman method in Section 2. Then in Section 3, a new model for the two-phase level set formulation is proposed, and we further extend it to the multi-phase and the vector-valued formulation. Meanwhile, the split Bregman method is applied to minimize the energy functionals of proposed model efficiently. Next, we apply our model to segment some synthetic and real medical images and give specific experimental results in Section 4. In Section 5, we make a concise summary for this paper.

2. Preparations

2.1. The LSE model

The LSE model, proposed by Li et al. in [16], is a novel model that can segment images and estimate the bias field at the same time, in which a local intensity cluster property is used to deal with the problem of intensity inhomogeneity. In the LSE model, the intensity inhomogeneity is considered as an inherent component of the image. Let Ω be the entire image domain, and $I: \Omega \to \Re$ be a given image. As a result, for a measured image I, it is accepted to establish the image model as follows:

$$I = bJ + n, \tag{1}$$

where b is a slowly varying bias field that explains the main reason of intensity inhomogeneity. J is the true image, which is seen as an ideal image approximated by a piecewise constant function. And n is generally the zero-mean Gaussian noise.

The image domain Ω is divided into N disjoint subregions $\{\Omega_i\}_{i=1}^{N}$ by the contour C, i.e. $\Omega = \bigcup_{i=1}^{N} \Omega_i$, and $\Omega_i \bigcap \Omega_j = \varnothing$ for $i \neq j$. By doing this, the ideal image J can be approximated by N distinct constants, denoted by $c_1, c_2, \ldots, c_N$.

Introducing a level set function ϕ, the energy functional proposed in the LSE model is:

$$F(\phi, \mathbf{c}, b) = E(\phi, \mathbf{c}, b) + \upsilon L(\phi) + \mu R(\phi), \tag{2}$$

where $E(\phi,\mathbf{c},b)$, $L(\phi)$, $R(\phi)$ are the data term, the length term and the regularization term, respectively, defined as

$$\begin{cases} E(\phi, \mathbf{c}, b) = \int\limits_{\Omega} \left(\sum_{i=1}^{N} \lambda_i \int K_\sigma(\mathbf{y} - \mathbf{x}) |I(\mathbf{x}) - b(\mathbf{y}) c_i|^2 dy M_i(\phi(\mathbf{x})) \right) d\mathbf{x}, \\ L(\phi) = \int\limits_{\Omega} |\nabla H_\epsilon(\phi)| d\mathbf{x}, \\ R(\phi) = \int\limits_{\Omega} \frac{1}{2} (|\nabla \phi| - 1)^2 d\mathbf{x}, \end{cases} \tag{3}$$

where $\mathbf{c}$ is a constant vector with $\mathbf{c} = (c_1, c_2, \ldots, c_N)$, $\mathbf{x} = (x,y)$, $\mathbf{y} = (s,t)$. λ_i, υ and μ are positive parameters. H_ϵ is a smooth function that approximates the Heaviside function, generally defined by

$$H_\epsilon(w) = \frac{1}{2}\left[1 + \frac{2}{\pi} \arctan\left(\frac{w}{\epsilon}\right)\right]. \tag{4}$$

and $M_i(\phi(\mathbf{x}))$ is the membership function of the regions Ω_i, i = 1,2,…,N, denoted by

$$M_i(\phi_1(\mathbf{x}), \phi_2(\mathbf{x}), \ldots, \phi_k(\mathbf{x})) = \begin{cases} 1, & \mathbf{x} \in \Omega_i, \\ 0, & \mathbf{x} \notin \Omega_i. \end{cases} \tag{5}$$

Taking ρ as the radius, K_σ is the Gaussian kernel function with σ as standard deviation, defined by

$$K_\sigma(\mathbf{x}) = \begin{cases} \frac{1}{2\pi\sigma^2} e^{-|\mathbf{x}|^2/2\sigma^2}, & |\mathbf{x}| \le \rho \\ 0, & \text{otherwise}, \end{cases} \tag{6}$$

where we choose $\rho = 4\sigma + 1$ in this paper.

2.2. The split Bregman method

The split Bregman method [23] is a quick way used to solve the L1-

regularized problems, which is required to have the following form:

$$\min_u (|R(u)|_1 + Q(u)) \tag{7}$$

where $|\cdot|_1$ represents the L1-norm, $R(\cdot)$ and $Q(\cdot)$ are two functionals.

By introducing an auxiliary variable $\mathbf{d}$, the following equivalent constrained problem is considered:

$$\min_{u,\mathbf{d}} (|\mathbf{d}|_1 + Q(u)) \quad \text{such that} \quad \mathbf{d} = R(u) \tag{8}$$

which is then converted to an unconstrained problem by adding a quadratic penalty function:

$$\min_{u,\mathbf{d}} \left(|\mathbf{d}|_1 + Q(u) + \frac{\lambda}{2} \|\mathbf{d} - R(u)\|^2 \right), \tag{9}$$

where λ is a positive parameter and $\|\cdot\|$ represent the L2-norm.

Because the penalty function only enforces the constraint $\mathbf{d} = R(u)$ weakly, the continuation method needs to use very large value for the penalty parameter λ, which may cause the problem of numerical instability. The split Bregman method can overcome this difficulty by applying the Bregman iteration to enforce the constraint $\mathbf{d} = R(u)$ strictly with a fixed value for λ. Specifically, the split Bregman iteration scheme for solving Eq. (7) or Eq. (8) can be explicitly expressed as follows:

$$(u^{k+1}, \mathbf{d}^{k+1}) = \arg\min_{u,\mathbf{d}} \left(|\mathbf{d}|_1 + Q(u) + \frac{\lambda}{2} \|\mathbf{d} - R(u) - \mathbf{b}^k\|^2 \right), \tag{10}$$

where $\mathbf{b}$ is an introduced Bregman variable, which can be updated by:

$$\mathbf{b}^{k+1} = \mathbf{b}^k + (R(u^{k+1}) - \mathbf{d}^{k+1}). \tag{11}$$

The most significant advantage of the split Bregman method is its efficiency in solving the above L1 regularized problems compared with traditional methods. Details about the split Bregman method and its advantages can be found in [23,24,31,32]. Later in this paper we will use this method to minimize our new energy functional more efficiently.

3. The main work

Although the LSE model can successfully achieve image segmentation and bias field estimation for inhomogenous images at the same time, its energy functional does not have the structure and properties that can be solved by the split Bregman method, thus the standard gradient descent method is used to minimize it, which results in much slower calculation speed. In this paper, we incorporate the bias field, the level set method and the global convex segmentation (GCS) method to propose a new model, in which the energy functional has the same particular form as the L1 regularization problem. Then we can apply the split Bregman method to minimize the energy functional, which can greatly improve the efficiency of the algorithm.

In this section, we mainly introduce our model in two parts: one is to establish the energy functionals in Subsection 3.1, including the two-phase, the multi-phase and the vector-valued formulation. The other is to minimize energy functionals applying the split Bregman method in Subsection 3.2.

3.1. The energy functional

3.1.1. Two-phase level set formulation

In order to establish the two-phase level set formulation, we set $N = 2$. That is, the entire image domain Ω is divided into two disjoint regions Ω_1 and Ω_2. By using a level set function ϕ, we can represent the two different regions by $\Omega_1 = \{\mathbf{x} : \phi(\mathbf{x}) > 0\}$ and $\Omega_2 = \{\mathbf{x} : \phi(\mathbf{x}) < 0\}$.

The energy functional in our proposed model is defined as:

$$F(\phi, \mathbf{c}, b) = \int_\Omega g(|\nabla I(\mathbf{x})|)|\nabla\phi(\mathbf{x})| d\mathbf{x} + \int_\Omega \phi(\mathbf{x}) r(\mathbf{x}) d\mathbf{x}, \tag{12}$$

where $\mathbf{c} = (c_1, c_2)$, g is a nonnegative edge detection function, which is introduced in detail below. $r(\mathbf{x})$ is defined as

$$r(\mathbf{x}) = \lambda_1 e_1 - \lambda_2 e_2, \tag{13}$$

where $e_i(\mathbf{x})$ is represented by

$$e_i(\mathbf{x}) = \int K_\sigma(\mathbf{y} - \mathbf{x}) |I(\mathbf{x}) - b(\mathbf{y}) c_i|^2 d\mathbf{y}, \quad i = 1, 2. \tag{14}$$

The first term on the right hand side of the Eq. (12) is called the weighted length term, which is mainly to regularize the length of contour as short as possible and to make the contour smoother. And the second term is the data fitting term, which attracts the contour to move towards the boundary and makes the segmentation results as accurate as possible.

Next we give a specific derivation process of the energy (12). Based on the LSE model, we choose $N = 2$, then the energy (2) becomes

$$\begin{aligned} P(\phi, \mathbf{c}, b) = & \int_\Omega \left(\sum_{i=1}^{2} \lambda_i \int K_\sigma(\mathbf{y} - \mathbf{x}) |I(\mathbf{x}) - b(\mathbf{y}) c_i|^2 d\mathbf{y} M_i(\phi(\mathbf{x})) \right) d\mathbf{x} \\ & + \upsilon \int_\Omega |\nabla H_\varepsilon(\phi)| d\mathbf{x} + \mu \int_\Omega \frac{1}{2} (|\nabla\phi| - 1)^2 d\mathbf{x}, \end{aligned} \tag{15}$$

where $M_1 = H_\epsilon(\phi)$, and $M_2 = 1 - H_\epsilon(\phi)$.

In order to get the result of image segmentation and estimate the bias field b, we should minimize the energy function in Eq. (15) with respect to $\mathbf{c}$, b and ϕ, respectively.

Keeping ϕ and b fixed, we minimize $P(\phi,\mathbf{c},b)$ in Eq. (15) with respect to $\mathbf{c}$ to obtain the optimal solution $\tilde{\mathbf{c}}$:

$$\tilde{c}_i = \frac{\int (b * K_\sigma) I M_i(\phi(\mathbf{y})) d\mathbf{y}}{\int (b^2 * K_\sigma) M_i(\phi(\mathbf{y})) d\mathbf{y}} \quad i = 1, 2. \tag{16}$$

Keeping ϕ and $\mathbf{c}$ fixed, we minimize $P(\phi,\mathbf{c},b)$ in Eq. (15) with respect to b to get the optimal solution $\tilde{b}$:

$$\tilde{b} = \frac{IJ^{(1)} * K_\sigma}{J^{(2)} * K_\sigma}, \tag{17}$$

where $J^{(1)} = \sum_{i=1}^{2} c_i M_i(\phi(\mathbf{y}))$ and $J^{(2)} = \sum_{i=1}^{2} c_i^2 M_i(\phi(\mathbf{y}))$.

In order to evolve the level set function ϕ to get the eventually contour, we minimize the energy function $P(\phi,\mathbf{c},b)$ in Eq. (15) with respect to ϕ with $\mathbf{c}$ and b fixed, and use the equation $\frac{\partial P}{\partial \phi} = -\frac{\partial \phi}{\partial t}$, we can get the following gradient flow equation:

$$\frac{\partial \phi}{\partial t} = -\delta_\varepsilon(\phi)(\lambda_1 e_1 - \lambda_2 e_2) + \upsilon \delta_\varepsilon(\phi) \mathrm{div}\left(\frac{\nabla\phi}{|\nabla\phi|} \right) + \mu \left(\nabla^2\phi - \mathrm{div}\left(\frac{\nabla\phi}{|\nabla\phi|} \right) \right), \tag{18}$$

where $e_i(\mathbf{x})$ is denoted in Eq. (14). And the Delta function δ_ϵ is defined as the derivative of H_ϵ, which can be computed by

$$\delta_\varepsilon = H'_\varepsilon(w) = \frac{1}{\pi} \frac{\varepsilon}{\varepsilon^2 + w^2}. \tag{19}$$

Due to the last term of Eq. (18), it is difficult for us to get the form suitable for solving with split Bregman method. Moreover, the last term of Eq. (18) is derived from $\mu \int \frac{1}{2} (|\nabla\phi| - 1)^2 d\mathbf{x}$ in Eq. (15) whose role is to maintain the regularity of the level set function. But this term has very little effect on the segmentation result. Consequently, it is reasonable for us to remove the last term from Eq. (18). Droping out the last term from Eq. (18) and setting $\upsilon = 1$, we can get the following equation:

$$\frac{\partial \phi}{\partial t} = -\delta_\varepsilon(\phi)(\lambda_1 e_1 - \lambda_2 e_2) + \delta_\varepsilon(\phi) \mathrm{div}\left(\frac{\nabla\phi}{|\nabla\phi|} \right). \tag{20}$$

By using the idea of the GCS method [33], we learn that the gradient flow Eq. (20) has the same stable solution with the following simplified equation:

$$\frac{\partial\phi}{\partial t} = -(\lambda_1 e_1 - \lambda_2 e_2) + \mathrm{div}\left(\frac{\nabla\phi}{|\nabla\phi|}\right). \tag{21}$$

Based on the simplified Eq. (21), we propose a new energy functional:

$$\bar{F}(\phi, \mathbf{c}, b) = \int_\Omega |\nabla\phi(\mathbf{x})| d\mathbf{x} + \int_\Omega \phi(\mathbf{x}) r(\mathbf{x}) d\mathbf{x}. \tag{22}$$

In addition, in order to detect the edge more easily, we introduce an edge function $g(|\nabla I(\mathbf{x})|)$, denoted by

$$g(|\nabla I(\mathbf{x})|) = \frac{1}{1 + \beta|\nabla I(\mathbf{x})|^2}, \tag{23}$$

where β is non-negative parameter, and for a gray image I, $|\nabla I(\mathbf{x})|^2$ is defined as

$$|\nabla I(\mathbf{x})|^2 = \left(\frac{\partial I}{\partial x}\right)^2 + \left(\frac{\partial I}{\partial y}\right)^2. \tag{24}$$

Adding the edge function $g(|\nabla I(\mathbf{x})|)$ into the first term of the energy functional (22), we get the eventual energy functional of the two-phase level set formulation in Eq. (12).

3.1.2. Multi-phase level set formulation

For those images with multiple regions, it is improper to segment them by using the two-phase formulation described above. As a result, we naturally need to extend our proposed method to the multi-phase level set formulation, which needs to use multiple level set functions. In this paper, in order to segment the brain MR images as accurately as possible, we mainly pay more attention to establishing the four-phase energy model. As described in [34], we know that n level set functions can represent 2^n disjoint regions at most. In such case, we prefer to choose two level set functions because they are enough for us to represent four disjoint regions.

In detail, we choose two level set functions ϕ_1 and ϕ_2 in this paper to denote the four regions by $\Omega_1 = \{\phi_1 > 0, \phi_2 > 0\}$, $\Omega_2 = \{\phi_1 > 0, \phi_2 < 0\}$, $\Omega_3 = \{\phi_1 < 0, \phi_2 > 0\}$ and $\Omega_4 = \{\phi_1 < 0, \phi_2 < 0\}$, respectively. Then using ϕ_1 and ϕ_2, we give the following energy functional of the multi-phase level set formulation for our proposed method:

$$\begin{aligned} F(\phi_1, \phi_2, \mathbf{c}, b) = {} & \upsilon\int_\Omega g(|\nabla I(\mathbf{x})|)|\nabla\phi_1(\mathbf{x})| d\mathbf{x} + \upsilon\int_\Omega g(|\nabla I(\mathbf{x})|)|\nabla\phi_2(\mathbf{x}) \\ & | d\mathbf{x} \\ & + \int_\Omega \phi_1(\mathbf{x}) T_1(\mathbf{x}) d\mathbf{x} + \int_\Omega \phi_2(\mathbf{x}) T_2(\mathbf{x}) d\mathbf{x}, \end{aligned} \tag{25}$$

where υ is a positive parameter, $\mathbf{c} = (c_1, c_2, c_3, c_4)$, and $T_1(\mathbf{x})$ and $T_2(\mathbf{x})$ are represented by:

$$\begin{cases} T_1(\mathbf{x}) = (\lambda_1 e_1 - \lambda_3 e_3) H_\epsilon(\phi_2) + (\lambda_2 e_2 - \lambda_4 e_4)(1 - H_\epsilon(\phi_2)), \\ T_2(\mathbf{x}) = (\lambda_1 e_1 - \lambda_2 e_2) H_\epsilon(\phi_1) + (\lambda_3 e_3 - \lambda_4 e_4)(1 - H_\epsilon(\phi_1)), \end{cases} \tag{26}$$

where λ_i (i = 1,2,3,4) is a positive constant, and $e_i(\mathbf{x})$ (i = 1,2,3,4) is defined the same as Eq. (14). Although $e_i(\mathbf{x})$ has the same expression form, there are still slight differences between the two formulas. In detail, the values of i are from 1 to 4 in the multi-phase formulation, while the values of i are only 1 and 2 in the two-phase formulation.

3.1.3. The vector-valued formulation

For color images, the image information is stored in multiple channels, and characteristics of the image are not complete in a single channel. In this case, if only one channel information is extracted to segment the color image, it may result in incorrect segmentation results with partial image information missing. In order to segment color images as well as possible, we modify the previous proposed model described in Section 3.1.1, and extend it naturally into the vector-valued formulation, in which the information of all channels is combined sufficiently to segment the color image accurately.

Assume there are M channels in color images, and let $\mathbf{I}$: $\Omega \rightarrow R^M$ be a given vector-valued image, and I_j (j = 1,2,⋯ ,M) are the M channels of the given image $\mathbf{I}$. Let b_j and c_j (j = 1,2,…,M) be the bias field and the average image intensity of the jth channel, respectively. For RGB images, there are three channels, that is $M = 3$. In this paper, for simplicity, we consider the RGB color images.

Taking the information of all channels into consideration, we modify the energy functional (12) to establish a new energy functional for color image as follows:

$$F(\phi, \mathbf{c}, b) = \int_\Omega g(|\nabla\mathbf{I}(\mathbf{x})|)|\nabla\phi(\mathbf{x})| d\mathbf{x} + \int_\Omega \phi(\mathbf{x}) \bar{r}(\mathbf{x}) d\mathbf{x}, \tag{27}$$

where $g(|\nabla\mathbf{I}(\mathbf{x})|)$ is the same edge function defined in Eq. (23), but different from Eq. (24), $|\nabla\mathbf{I}(\mathbf{x})|$ for a color image $\mathbf{I}$ in Eq. (27) is calculated by:

$$|\nabla\mathbf{I}(\mathbf{x})|^2 = \left(\frac{\partial I_1}{\partial x}\right)^2 + \left(\frac{\partial I_1}{\partial y}\right)^2 + \left(\frac{\partial I_2}{\partial x}\right)^2 + \left(\frac{\partial I_2}{\partial y}\right)^2 + \left(\frac{\partial I_3}{\partial x}\right)^2 + \left(\frac{\partial I_3}{\partial y}\right)^2, \tag{28}$$

and the function $\bar{r}(\mathbf{x})$ in Eq. (27) is defined as:

$$\bar{r}(\mathbf{x}) = \frac{1}{3}\sum_{j=1}^{3} (\lambda_{j,1} e_{j,1} - \lambda_{j,2} e_{j,2}), \tag{29}$$

where $\lambda_{j,1}$, $\lambda_{j,2}$ are two positive parameters in the jth channel. $e_{j,i}$ is denoted by

$$e_{j,i}(\mathbf{x}) = \int_\Omega K_\sigma(\mathbf{y} - \mathbf{x})|I_j(\mathbf{x}) - b_j(\mathbf{y}) c_{j,i}|^2 d\mathbf{y}, \quad i = 1, 2. \quad j = 1, 2, 3. \tag{30}$$

3.2. Minimization process by applying the split Bregman method

3.2.1. Minimization process for the two-phase formulation

In this paper, in order to minimize the energy functional (12), we limit ϕ in the interval [-2,2] for the two-phase formulation to make convergence faster. The minimization process can be performed by:

$$\min_{-2\leqslant\phi\leqslant2} F(\phi) = \min_{-2\leqslant\phi\leqslant2} \left[\int_\Omega g(|\nabla I(\mathbf{x})|)|\nabla\phi(\mathbf{x})| d\mathbf{x} + \int_\Omega \phi(\mathbf{x}) r(\mathbf{x}) d\mathbf{x}\right]. \tag{31}$$

The minimization problem (31) can be simplified as follows:

$$\min_{-2\leqslant\phi\leqslant2} F(\phi) = \min_{-2\leqslant\phi\leqslant2} [|\nabla\phi|_g + \langle\phi, r\rangle], \tag{32}$$

where $|\cdot|_g$ and $\langle\cdot\rangle$ represent the weighted L1 norm and the inner product, respectively, defined as follows:

$$\begin{cases} |\nabla\phi|_g = \int_\Omega (g(|\nabla I(\mathbf{x})|)|\nabla\phi(\mathbf{x})|) d\mathbf{x}, \\ \langle\phi, r\rangle = \int_\Omega (\phi(\mathbf{x}) r(\mathbf{x})) d\mathbf{x}. \end{cases} \tag{33}$$

It is obvious that the minimization problem (32) is suitable to be solved by the split Bregman method introduced in Section 2.2. Next we give the solving process in detail.

By introducing an additional variable $\mathbf{d} = (d_x, d_y)$ and adding a quadratic penalty functional to the energy to approximately enforce $\mathbf{d} = \nabla\phi$, we can convert Eq. (32) to the following unconstrained optimization problems:

$$(\phi^*, \mathbf{d}^*) = \arg\min_{\substack{-2\leqslant\phi\leqslant2 \\ \mathbf{d}}} \left[|\mathbf{d}|_g + \langle\phi, r\rangle + \frac{\lambda}{2}\|\mathbf{d} - \nabla\phi\|^2\right], \tag{34}$$

where λ is a fixed positive parameter.

In order to make the equality $\mathbf{d} = \nabla\phi$ be strictly true, we apply the Bregman iteration to Eq. (34) by adding a Bregman variable $\mathbf{m} = (m_x, m_y)$, such that we obtain a series of unconstrained optimization problems and Bregman iterations as follows:

$$(\phi^{k+1}, \mathbf{d}^{k+1}) = \arg \min_{\substack{-2\leqslant\phi\leqslant 2\\ \mathbf{d}}} \left[|\mathbf{d}|_g + \langle \phi, r\rangle + \frac{\lambda}{2}\|\mathbf{d} - \nabla\phi - \mathbf{m}^k\|^2 \right], \tag{35}$$

where $\mathbf{m}^{k+1}$ is updated by

$$\mathbf{m}^{k+1} = \mathbf{m}^k + (\nabla\phi^{k+1} - \mathbf{d}^{k+1}). \tag{36}$$

What's more important, it is not to be ignored that ϕ^{k+1} and $\mathbf{d}^{k+1}$ obtained by the minimization problem (35) converge to ϕ^* and $\mathbf{d}^*$ in the sense of L2 norm, respectively. To express in a mathematical language, that is to say, $\lim_{k\to\infty} \|\phi^{k+1} - \phi^*\| = 0$ and $\lim_{k\to\infty} \|\mathbf{d}^{k+1} - \mathbf{d}^*\| = 0$. The correctness of this conclusion has been proved successfully by Yang et al., and the detailed process of proof can be referred to [35].

In order to evolve ϕ to get the final contour, we need to minimize Eq. (35) with respect to ϕ for fixed $\mathbf{d}$:

$$\phi^{k+1} = \arg \min_{-2\leqslant\phi\leqslant 2} \left[\langle \phi, r^k\rangle + \frac{\lambda}{2}\|\mathbf{d}^k - \nabla\phi - \mathbf{m}^k\|^2 \right]. \tag{37}$$

Solving the minimization problem (37), we can get the following Euler-Lagrange equation:

$$\triangle\phi^{k+1} = \frac{r^k}{\lambda} + \nabla\cdot(\mathbf{d}^k - \mathbf{m}^k), \quad \text{whenever} \quad -2 \leq \phi^k \leq 2. \tag{38}$$

Making use of the finite different method, we use the central difference to approximate $\triangle\phi^{k+1}$ and use the backward difference to approximate $\nabla\cdot(\mathbf{d}^k - \mathbf{m}^k)$, we discretize the problem (38) into the following scheme, which is also the iteration scheme for ϕ^{k+1}.

$$\begin{cases} a_{i,j}^k = d_{x,i-1,j}^k - d_{x,i,j}^k + d_{y,i,j-1}^k - d_{y,i,j}^k, \\ p_{i,j}^k = a_{i,j}^k - (m_{x,i-1,j}^k - m_{x,i,j}^k + m_{y,i,j-1}^k - m_{y,i,j}^k), \\ q_{i,j}^k = \dfrac{1}{4}\left(\phi_{i-1,j}^k + \phi_{i+1,j}^k + \phi_{i,j-1}^k + \phi_{i,j+1}^k - \dfrac{1}{\lambda} r_{i,j}^k + p_{i,j}^k\right), \\ \phi_{i,j}^{k+1} = \max\left\{\min\left\{\overset{k}{\underset{i,j}{q}}, 2\right\}, -2\right\}. \end{cases} \tag{39}$$

Keeping ϕ fixed, we minimize Eq. (35) with respect to $\mathbf{d}$. We need to solve the following minimization problem:

$$\mathbf{d}^{k+1} = \arg \min_{\mathbf{d}} \left[|\mathbf{d}|_g + \frac{\lambda}{2}\|\mathbf{d} - \nabla\phi^{k+1} - \mathbf{m}^k\|^2 \right]. \tag{40}$$

Through calculating the minimization problem (40), we can get the optimal solution as follows:

$$\begin{aligned} \mathbf{d}^{k+1} &= \text{shrink}_g\left(\mathbf{m}^k + \nabla\phi^{k+1}, \frac{1}{\lambda}\right) \\ &= \text{shrink}\left(\mathbf{m}^k + \nabla\phi^{k+1}, \frac{g}{\lambda}\right), \end{aligned} \tag{41}$$

where shrink($\mathbf{z}$,r) is the vector shrinkage operator and it can be represented by

$$\text{shrink}(\mathbf{z}, r) = \begin{cases} \dfrac{\mathbf{z}}{|\mathbf{z}|}\max(|\mathbf{z}| - r, 0), & \mathbf{z} \neq \mathbf{0} \\ 0, & \mathbf{z} = \mathbf{0}. \end{cases} \tag{42}$$

At the same time, it is worth noting that before updating ϕ in each iteration, we must update $\mathbf{c} = (c_1, c_2)$ and b through Eqs. (16) and (17), respectively.

3.2.2. Minimization process for the multi-phase formulation

When we minimize the energy (25), we prefer to limit both ϕ_1 and ϕ_2 to the interval [-2,2] to accelerate the speed of convergence and to get the global minimizer. Meanwhile, we simplify the minimization problem as follows:

$$\begin{aligned} \min_{-2\leqslant\phi_1,\phi_2\leqslant 2} F(\phi_1, \phi_2, \mathbf{c}, b) = \min_{-2\leqslant\phi_1,\phi_2\leqslant 2} &[\upsilon|\nabla\phi_1|_g + \upsilon|\nabla\phi_2|_g \\ &+ \langle\phi_1, T_1\rangle + \langle\phi_2, T_2\rangle], \end{aligned} \tag{43}$$

where $|\cdot|_g$ and $\langle\cdot\rangle$ are the weighted L1 norm and the inner product defined in Eq. (33).

Analogous to the solving process of the two phase formulation, the split Bregman method is applied into the multi-phase level set formulation. Introducing auxiliary variables $\mathbf{d}_1$, $\mathbf{d}_2$, $\mathbf{m}_1$ and $\mathbf{m}_2$, the minimization problem (43) can eventually be transformed into the following scheme:

$$\begin{aligned} (\phi_1^{k+1}, \phi_2^{k+1}, \mathbf{d}_1^{k+1}, \mathbf{d}_2^{k+1}) = \arg \min_{\substack{-2\leqslant\phi\leqslant 2\\ \mathbf{d}_1,\mathbf{d}_2}} &(\upsilon|\mathbf{d}_1|_g + \upsilon|\mathbf{d}_2|_g + \langle\phi_1, T_1\rangle + \langle\phi_2, T_2\rangle \\ &+ \frac{\lambda}{2}\|\mathbf{d}_1 - \nabla\phi_1 - \mathbf{m}_1^k\|^2 + \frac{\lambda}{2}\|\mathbf{d}_2 - \nabla\phi_2 - \mathbf{m}_2^k\|^2\Big), \end{aligned} \tag{44}$$

where $\mathbf{m}_l^{k+1}$ is updated by

$$\mathbf{m}_l^{k+1} = \mathbf{m}_l^k + (\nabla\phi_l^{k+1} - \mathbf{d}_l^{k+1}), =1, 2. \tag{45}$$

Minimizing Eq. (44) with respect to ϕ_l for fixed $\mathbf{d}_1$ and $\mathbf{d}_2$, we obtain the following Euler-Lagrange equation:

$$\begin{aligned} \triangle\phi_l^{k+1} = \frac{T_l^k}{\lambda} + \nabla\cdot(\mathbf{d}_l^k - \mathbf{m}_l^k), \quad \text{whenever} \quad -2 \leq \phi_l^k \leq 2, \quad l \\ = 1, 2. \end{aligned} \tag{46}$$

Using the same finite difference method as described in Section 3.1.1, we discretize the problem (46) into the following numerical iteration scheme for updating ϕ_l ($l = 1,2$):

$$\begin{cases} a_{l,i,j}^k = d_{x,l,i-1,j}^k - d_{x,l,i,j}^k + d_{y,l,i,j-1}^k - d_{y,l,i,j}^k, \\ p_{l,i,j}^k = a_{l,i,j}^k - (m_{x,l,i-1,j}^k - m_{x,l,i,j}^k + m_{y,l,i,j-1}^k - m_{y,l,i,j}^k), \\ q_{l,i,j}^k = \dfrac{1}{4}\left(\phi_{l,i-1,j}^k + \phi_{l,i+1,j}^k + \phi_{l,i,j-1}^k + \phi_{l,i,j+1}^k - \dfrac{1}{\lambda} T_{l,i,j}^k + p_{l,i,j}^k\right), \\ \phi_{l,i,j}^{k+1} = \max\left\{\min\left\{\overset{k}{\underset{l,i,j}{q}}, 2\right\}, -2\right\}. \end{cases} \tag{47}$$

Keeping ϕ_1 and ϕ_2 fixed, we minimize Eq. (44) with respect to $\mathbf{d}_l$($l = 1,2$) to get the optimal solution as follows:

$$\begin{aligned} \mathbf{d}_l^{k+1} &= \text{shrink}_g\left(\mathbf{m}_l^k + \nabla\phi_l^{k+1}, \frac{\upsilon}{\lambda}\right) \\ &= \text{shrink}\left(\mathbf{m}_l^k + \nabla\phi_l^{k+1}, \frac{\upsilon}{\lambda}g\right), \end{aligned} \tag{48}$$

where shrink($\mathbf{z}$,r) is the vector shrinkage operator described in Eq. (42).

Likewise, we should pay more attention that we must update $\mathbf{c} = (c_1, c_2, c_3, c_4)$ and b through Eqs. (16) and (17) with $i = 1,2,3,4$ for the multi-phase formulation before updating ϕ_1 and ϕ_2, respectively. The only difference between the formulations in the specific update process is that the value of i is not the same. Specifically, when we update $\mathbf{c}$ and b for the multi-phase formulation, the value of i is set to $i = 1,2,3,4$ rather than $i = 1,2$ for the two-phase formulation. Meanwhile, it is worth noting that when we update b for the multi-phase formulation, $J^{(1)}$ and $J^{(2)}$ of Eq. (17) become $J^{(1)} = \sum_{i=1}^4 c_i M_i(\phi(\mathbf{y}))$ and $J^{(2)} = \sum_{i=1}^4 c_i^2 M_i(\phi(\mathbf{y}))$, respectively.

3.2.3. Minimization process for the vector-valued formulation

In the two-phase formulation, we limit ϕ to [-2,2], here we choose to let ϕ take a value in [-1,1] to make the speed of convergence faster. Meanwhile, comparing the two-phase formulation and the vector-valued formulation, we find that their energy functional is very similar, and the only difference is the way to calculate $r(\mathbf{x})$ in the data fitting term. Specifically, $r(\mathbf{x})$ in Eq. (13) of the two-phase formulation is replaced by $\bar{r}(\mathbf{x})$ defined by Eq. (29) in the vector-valued formulation. However, the slight difference in the calculation way will not affect the entire minimization process. Consequently, the process of using the split Bregman method to minimize the vector-valued formulation is the same as the minimization process of the two-phase formulation. For this reason, we only give the final iterative scheme for minimizing the energy in the vector-valued formulation as follows:

$$\begin{cases} a_{i,j}^{k} = d_{x,i-1,j}^{k} - d_{x,i,j}^{k} + d_{y,i,j-1}^{k} - d_{y,i,j}^{k}, \\ p_{i,j}^{k} = a_{i,j}^{k} - (m_{x,i-1,j}^{k} - m_{x,i,j}^{k} + m_{y,i,j-1}^{k} - m_{y,i,j}^{k}), \\ q_{i,j}^{k} = \frac{1}{4}\left(\phi_{i-1,j}^{k} + \phi_{i+1,j}^{k} + \phi_{i,j-1}^{k} + \phi_{i,j+1}^{k} - \frac{1}{\lambda}\bar{r}_{i,j}^{k} + p_{i,j}^{k}\right), \\ \phi_{i,j}^{k+1} = \max\left\{\min\left\{\overset{k}{\underset{i,j}{q}}, 1\right\}, -1\right\}. \end{cases} \tag{49}$$

In the above iteration scheme, **m** and **d** are iterated by the same format as Eqs. (36) and (41). In each iteration, we should pay more attention that we must update b and $\mathbf{c}$ through Eqs. (50) and (51) before updating ϕ.

$$\widetilde{b_j} = \frac{(I_j J_j^{(1)})^{*} K_\sigma}{J_j^{(2)*} K_\sigma}, \quad j = 1, 2, 3, \tag{50}$$

where $J_j^{(1)} = \sum_{i=1}^{2} c_{j,i} M_i(\phi(\mathbf{y}))$ and $J_j^{(2)} = \sum_{i=1}^{2} c_{j,i}^{2} M_i(\phi(\mathbf{y}))$.

$$\widetilde{c_{j,i}} = \frac{\int (b_j{}^{*} K_\sigma) I_j M_i(\phi(\mathbf{y})) d\mathbf{y}}{\int (b_j^{2}{}^{*} K_\sigma) M_i(\phi(\mathbf{y})) d\mathbf{y}} \quad i = 1, 2. \qquad j = 1, 2, 3. \tag{51}$$

4. Experimental results

In this part, we mainly use the proposed model to segment a total of 91 synthetic and real MR images with intensity inhomogeneity, including the two-phase, multi-phase and color images, and further exhibit their segmentation results, the estimated bias fields and the bias correction images.

4.1. Experimental results for two-phase images

In this part, we mainly show some experimental results for two-phase images. For all two-phase MR images, we almost select the same parameter settings. In detail, we set the scale parameter $\sigma = 20.0$, $\epsilon = 1$ and $\lambda = 1$ in quadratic penalty function. In the experiment, the sizes of images in Fig. 1 are 123 × 120, 123 × 120, 191 × 153 and 169 × 204. Besides, the sizes of all synthetic images used in our experiments are 90 × 90. To verify the accuracy and efficiency of our model, we also apply the LSE model and the MICO model to segment MR images and further quantitatively compared their experimental results.

In order to quantitatively evaluate the segmentation accuracy and the correction effect, we introduce two evaluation criteria: the Dice similarity coefficient (Dice) and the coefficient of variations (CV). The Dice value is a similarity metric to evaluate the segmentation accuracy, which is defined as follows:

$$Dice(S_1, S_2) = \frac{2N(S_1 \bigcap S_2)}{N(S_1) + N(S_2)}, \tag{52}$$

where $N(\cdot)$ denotes the number of voxels on the closed set, S_1 denotes the region segmented by the model, S_2 denotes the truth region in general. The closer the Dice value is to 1, the more accurate the segmentation result is.

The CV value is an effective measure to evaluate the correction effect, which is defined as:

$$CV = \frac{\sigma(Z)}{\mu(Z)}, \tag{53}$$

where Z denotes the target region. σ represents the standard deviation of the intensity in the region, and μ is the average of the intensity in the region. In general, the smaller the CV value is, the more homogeneous the image is and the better the correction effect is.

We apply our model to segment 8 different heart MR images with intensity inhomogeneity, all of which are downloaded from the RV Segmentation Challenge in Cardiac MRI at http://www.litislab.fr/?projet=1rvsc. For simplicity, we only show 4 representative experimental results in Fig. 1. Row 1 to Row 4 in Fig. 1 are 4 different heart MR images to be segmented. And original images with initial contours, segmentation results, the estimated bias field and the bias correction images are shown in Column 1 to Column 4, respectively. From Column 2 in Fig. 1, it is obvious to see that our model can accurately segment these inhomogeneous heart MR images. Meanwhile, as shown as the correction images in Column 4, our model succeeds in eliminating the effects of the bias field such that the bias correction images are homogeneous enough.

In order to compare the accuracy of our model and the LSE model, we also apply the LSE model to segment the same heart MR images with the same initial contours as our method and show their results in Fig. 2. Due to the inhomogeneity and complexity of the heart MR images, we cannot intuitively compare the quality of both models by eyes. As a consequence, we choose the segmentation results of synthetic images, as shown in Fig. 4, to compare the accuracy of our model and the LSE model.

In addition to the LSE model, we also apply the CV model, the RSF model and the LGIF model to segment the same heart MR images as our model. To facilitate the comparison of the segmentation accuracy of these 4 models, we simultaneously show their segmentation results in Fig. 3. In this experiment, all models use the same initial contour. Original images with the initial contour is shown in Column 1, while Column 2 to Column 5 are the segmentation results of the CV model, the RSF model, the LGIF model and our model, respectively. By comparison, our model is significantly more accurate than the RSF model. Moreover, our model is more precise than the CV model and the LGIF model in terms of detail processing.

To compare the correction results of the LSE model and our model, we introduce the variance metric to quantitatively evaluate the correction effect. The variance value used in this paper is to calculate the variance for the entire image intensity. The smaller the variance value is, the more homogeneous the image is, which indicates that the effect of bias field correction is better. Here, we calculate the variance of original images and bias correction images obtained by the LSE model and our model, and record them in Table 1. Comparing the data in Table 1, it's easy to find that the variance of bias correction images obtained by our model is significantly lower than that of original images, from which we conclude that our model can well weaken the phenomenon of intensity inhomogeneity in the original image. In addition, the variance of bias correction images obtained by our model is also smaller than that of the LSE model, which further illustrates that the correction effect of our model is better than the LSE model.

To verify the efficiency of our method, we also record the CPU time of the LSE model and our model in Table 2 when we segment the same heart MR images in Fig. 1. Observing the CPU time in Table 2, we can find that compared with the LSE model, our model takes significantly less time when segmenting the same image, which demonstrates that our model is more efficient than the LSE model.

In Fig. 4, we synthesize a total of 30 synthetic images with intensity inhomogeneity by ourselves, and then use them to test the sensitivity of the LSE model and our model to the initial contour and noise, respectively. Among them, Row 1 to Row 3 are the experiment results of our model and the LSE model for different initial contours, while Row 4 to Row 6 are the experiment results of our model and the LSE model for different noises. Then, we analyze these experimental results in two aspects.

On the one hand, we first analyze the sensitivity of the LSE model and our model to the initial contour. In Fig. 4, Row 1 shows five original

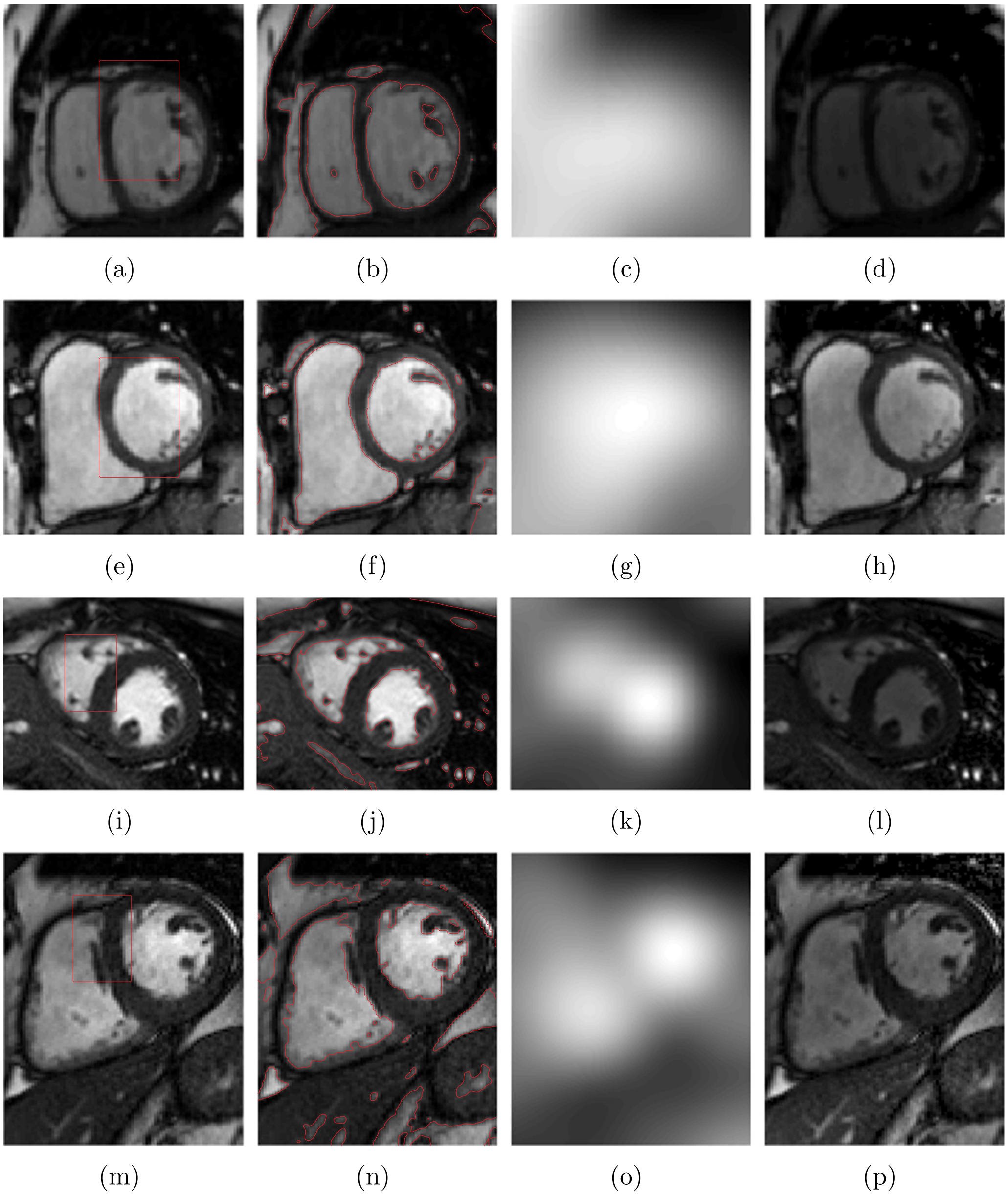

Fig. 1. Applications of our model to segment 4 different heart MR images. Column 1: Original images with initial contours; Column 2: Segmentation results; Column 3: The estimated bias fields; Column 4: The bias field correction images. $\sigma = 20$, $\beta = 10$, $\lambda_1 = \lambda_2 = 2 \times 10^{-6}$.

synthetic images with different initial contours, in which the former three images have the same intensity distribution but with different initial contours, while the fourth and fifth images not only have different initial contours but also differ from the former three images in intensity distribution. Row 2 and Row 3 represent the corresponding segmentation results of the LSE model and our model, respectively. From the segmentation results, we can see that our model can accurately segment the inhomogeneous images with different initial contours, but the LSE model gives incorrect segmentation results when dealing with such images, which demonstrates that our method is superior to the LSE model and is not sensitive to initial contours.

On the other hand, we analyze the effect of noise on our model. Here, we apply our model and the LSE model to segment the same synthetic images with different Gaussian or random noises. In Fig. 4, original synthetic images with the same initial contour but different noises are shown in Row 4, and the corresponding segmentation results of the LSE model and our model are shown in Row 5 and Row 6, respectively. It can be seen that even if the images are polluted by noise, our model can still segment them accurately, but the LSE model is disturbed by noise to give incorrect segmentation results, which further illustrates that our model is robust to noises. In conclusion, experimental results in Fig. 4 demonstrate that our model is not only insensitive to initial contours, but also robust to noises.

In order to quantitatively compare the segmentation accuracy of the LSE model and our model, we calculate the Dice values of the two models for different initial contours and different noises, respectively, and plot them as the scatter plots in Fig. 5. Fig. 5 (a) is the Dice values obtained by our model and the LSE model for different initial contours. It shows that the Dice values of our model are equal to 1, and are far greater than those of the LSE model, which demonstrates that our model is superior to the LSE model, and is not sensitive to initial contours. In addition, Fig. 5 (b) shows the scatter plot of the Dice values for different noises. Similarly, we can see that the Dice values of our model are always equal to 1 that are much larger than those of the LSE model, from which we conclude that our model gives completely accurate segmentation results for images with different noise. As a consequence,

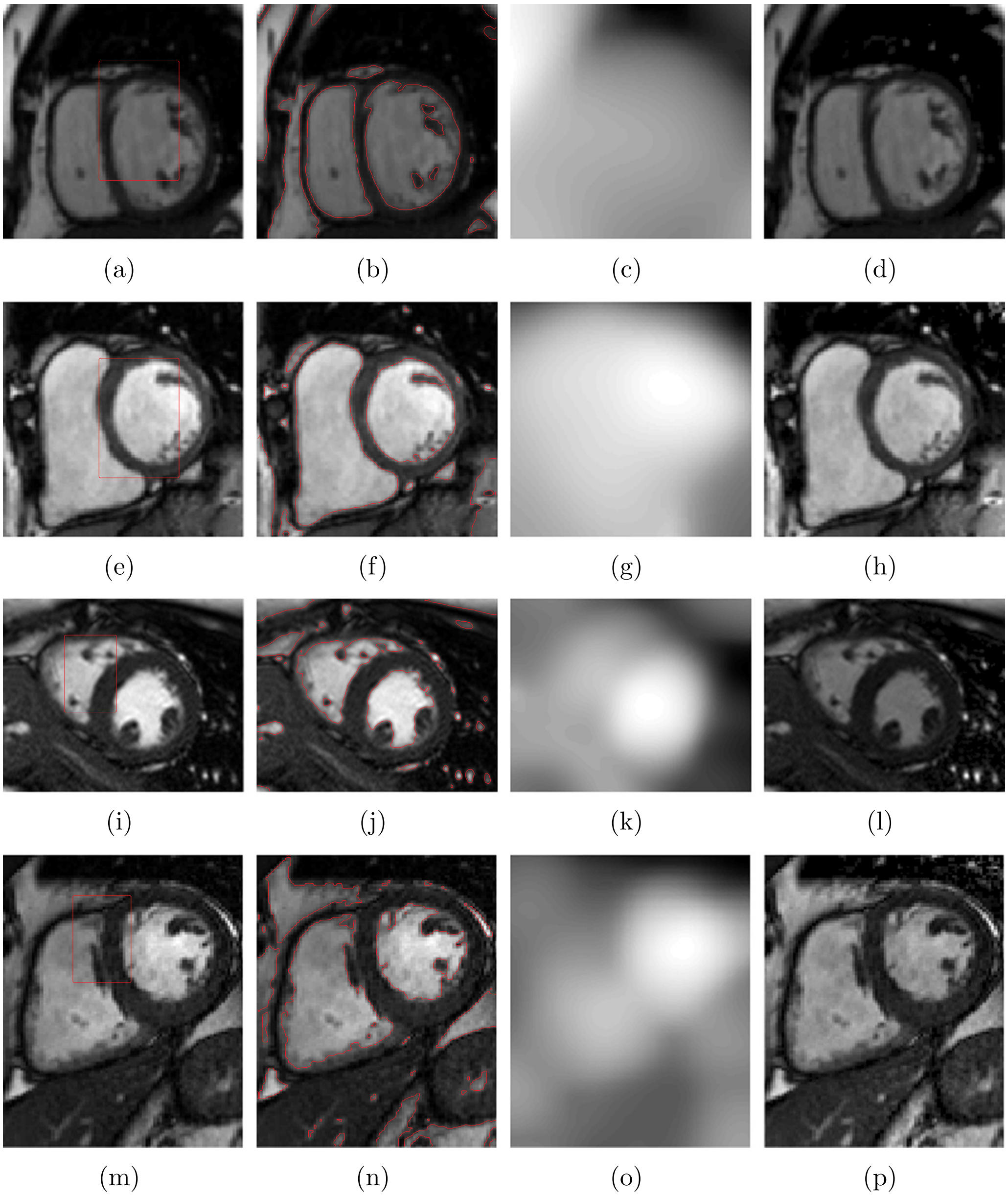

Fig. 2. Applications of the LSE model to segment 4 different heart MR images. Column 1: Original images with initial contours; Column 2: Segmentation results; Column 3: The estimated bias fields; Column 4: The bias field correction images. $\sigma = 15$, $\mu = 1$, $\nu = 0.001 \times 255^2$.

Fig. 5 quantitatively verifies that our model is not sensitive to initial contours, and is robust to noises.

4.2. Experimental results for multi-phase images

Brain and heart MR images are typical multi-phase images with intensity inhomogeneity, which is suitable to test accuracy of our multi-phase model in segmentation and correction. In this section, a total of 4 heart MR images and 43 brain MR images are used to test our model. Besides, in order to quantitatively analyze the segmentation accuracy and the correction effect of our model, we calculate the Dice values and the CV values to evaluate them, respectively.

In Fig. 6, three real brain MR images with intensity inhomogeneity are segmented and corrected by our model, which are downloaded from International Open Challenge Competition named MR Brain Image Segmentation 2013 at https://grand-challenge.org/challenges/. Original brain MR images, segmentation results, bias correction images, and the estimated bias are shown from Column 1 to Column 4, respectively. From the experimental results shown in Fig. 6, we can see that our model can accurately segment the white matter (WM), the gray matter (GM) and the cerebrospinal fluid (CSF). What's more, the bias correction images are more homogeneous and clear. All of these indicate that our model has a good performance in dealing with inhomogeneous images corrupted with bias field.

In the human heart MR image, the intensities of the left atrium and the left ventricle are similar to those of the myocardial wall due to imaging device, which creates a great difficulty in segmenting heart images. In this paper, we download the human heart MR images with intensity inhomogeneity from Grand Challenges in Biomedical Image Analysis at https://grand-challenge.org/challenges/, and then apply our model to segment and correct them. Specific experimental results are shown in Fig. 7. Column 1 to Column 4 are original images, segmentation images, bias correction images, and estimated bias, respectively. Observing the segmentation results in Column 2, we find that our model accurately segments the left atrium and the left ventricle. Besides, from the bias correction images shown in Column 3, it is

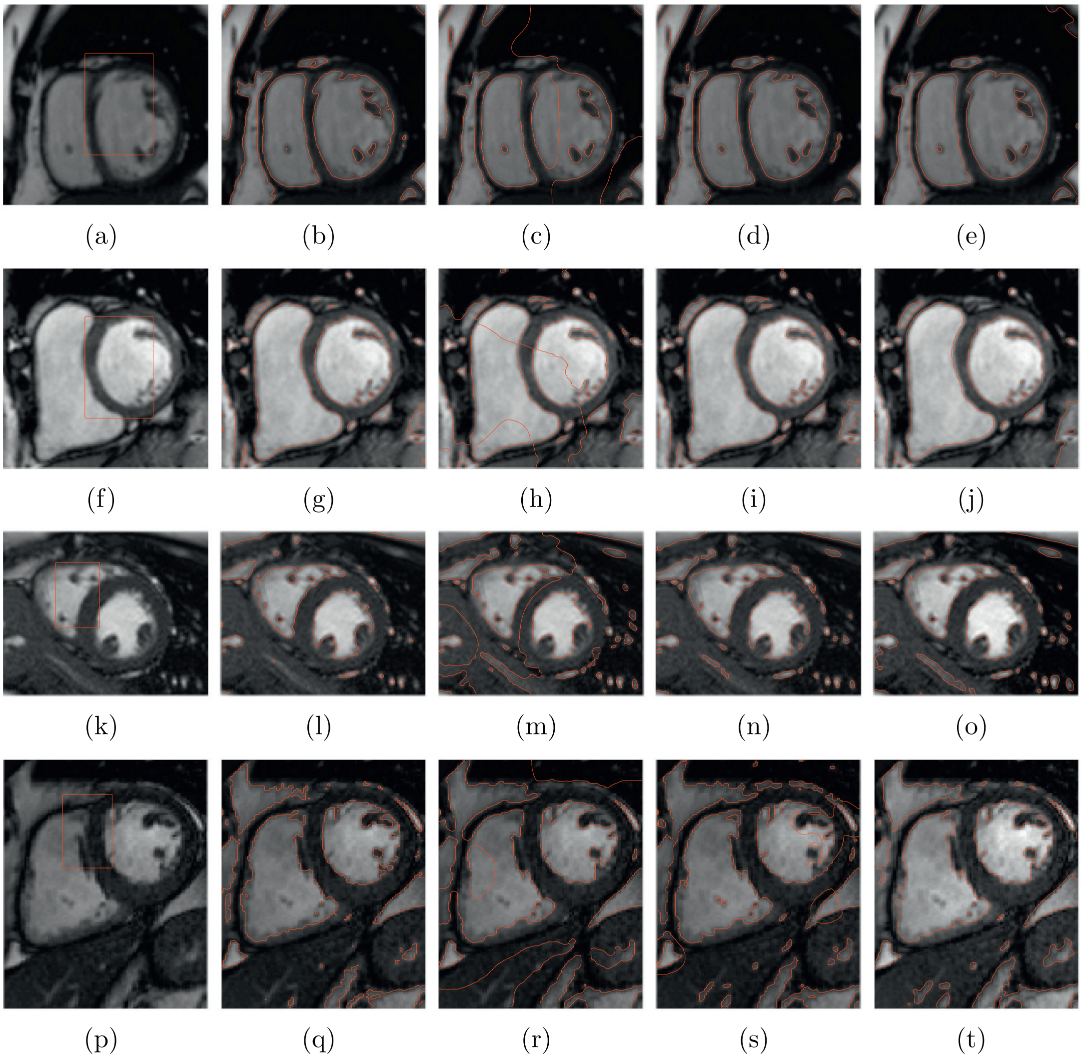

Fig. 3. Comparison results of the CV model, the RSF model, the LGIF model and our model to segment the same heart MR images in Fig. 1. Column 1: Original images with initial contours. Column 2: The CV model. Column 3: The RSF model. Column 4: The LGIF model. Column 5: Our model.

obvious that the bias field correction successfully eliminates the characteristic of intensity inhomogeneity and improves the intensity of the left atrium and the left ventricle, making them look clearer.

In order to test the effect of our model in bias correction, we provide the intensity distribution of original images and bias correction images which are listed in the Column 1 and Column 3 of Fig. 7, respectively. In Fig. 8, the histogram is a tool for us to show the intensity distribution of each image. In each subfigure, the left is the intensity histogram of the original image, and the right is the intensity histogram of the bias correction image. Through comparative analysis, the intensity distribution of the original image is relatively scattered and usually contains 3 distinct peaks representing the intensities of the left atrium, the left ventricle and the myocardial wall, which indicates that the intensity in the original image varies greatly such that the original image is very inhomogeneous. However, there are only two distinct peaks in the intensity histogram of the bias correction image, one representing the intensity of the left atrium and the left ventricle, and the other representing the intensity of the myocardial wall. This is because our model has the ability to eliminate the adverse effects of bias and corrects the intensity of the left ventricle and the left atriums to be very close. Although there are still three obvious peaks in Fig. 8 (c), it is more concentrated than that of the original image, indicating that the bias correction image is more homogeneous than the original image. As a consequence, comparison of the intensity histogram quantitatively demonstrates that the correction effect of our model is satisfactory.

In order to test the performance of our model for brain MR images, we apply our model to segment a total of forty brain MR images with intensity inhomogeneities, and then calculate the Dice values and the CV values to evaluate the segmentation accuracy and the correction effect, respectively. All brain MR images and their groundtruths are downloaded from International Open Challenge Competition named MR Brain Image Segmentation 2013 at https://grand-challenge.org/challenges/. The initial contours of all images are random. In Fig. 9, instead of showing all experimental results, we only give the segmentation results of our model for four representative images, which are selected from forty brain MR images. Original images, segmentation results, bias correction images and bias fields are displayed from Column 1 to Column 4, respectively. Observing and analyzing the segmentation results, we find that WM is accurately segmented by the internal red contour, while the blue contour exactly detects the area of GM. On the other hand, from the bias correction images, our model increases the intensity of the darker area in the original image to eliminate the negative effects of the bias field, that's why bias correction images look more homogeneous and clearer. All of these illustrate that our model has extremely satisfying results for brain MR images.

The Dice value is an effective metric for quantitative analysis of segmentation accuracy. Here, in order to quantitatively compare the LSE model, the MICO model and our model, we apply the LSE model

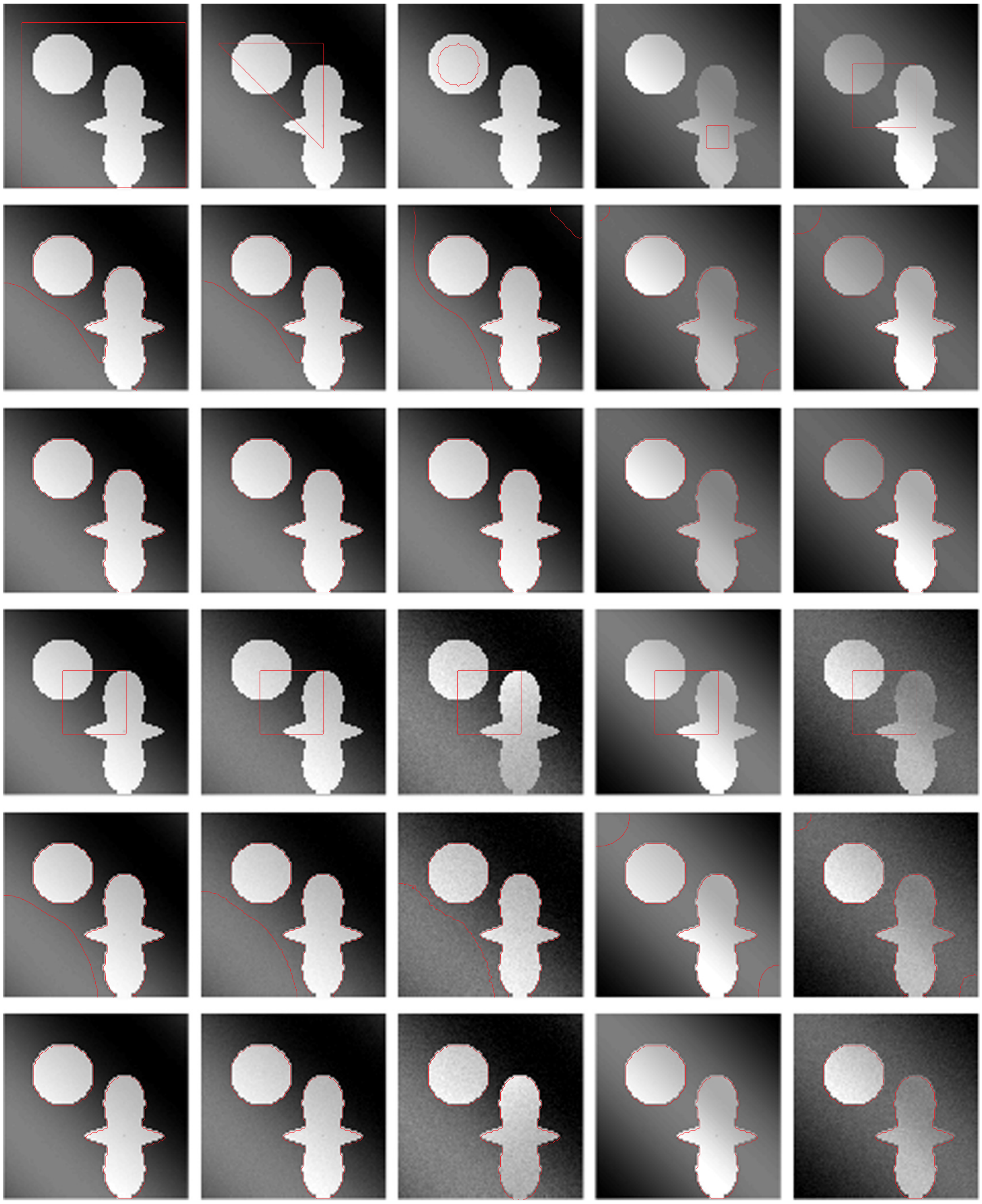

Fig. 4. Segmentation results of the LSE model and our method for 10 synthetic images with severe intensity inhomogeneity. Row 1: Original images with different initial contours. Row 2: Segmentation results of the LSE model. Row 3: Segmentation results of our model. Row 4: Original images with the same initial contour but different Gaussian or random noises. Row 5: Segmentation results of the LSE model. Row 6: Segmentation results of our model.

Table 1
Comparison of the variance of the bias correction images with the LSE model and our model. (* 10^3, unit: pixel).

	Fig. 1 (a)	Fig. 1 (e)	Fig. 1 (i)	Fig. 1 (m)
Original images	5.253	8.501	8.261	7.215
LSE model	3.512	5.208	6.846	6.994
Our model	2.509	5.180	3.850	6.588

Table 2
Comparison of the CPU time with the LSE model and our model to segment the same images in Figs. 1 and 2. (unit: second).

	Fig. 1 (a)	Fig. 1 (e)	Fig. 1 (i)	Fig. 1 (m)
LSE model	2.572	2.363	3.422	3.849
Our model	0.416	0.428	0.940	1.130

and the MICO model to segment the same forty brain MR images as our model, respectively, and then calculate their Dice values to evaluate the segmentation accuracy. In Fig. 10, we specifically show the box plots for the Dice values. Column 1 to Column 3 represent the Dice values of CSF, GM and WM, respectively. As can be seen from the three box plots, whether WM, GM or CSF, Dice values of our model are obviously higher than those of the LSE model and the MICO model. In detail, for WM, the median, the lower quartile and the upper quartile of the Dice values for our model are 0.8689, 0.8347 and 0.9146, respectively, while those of

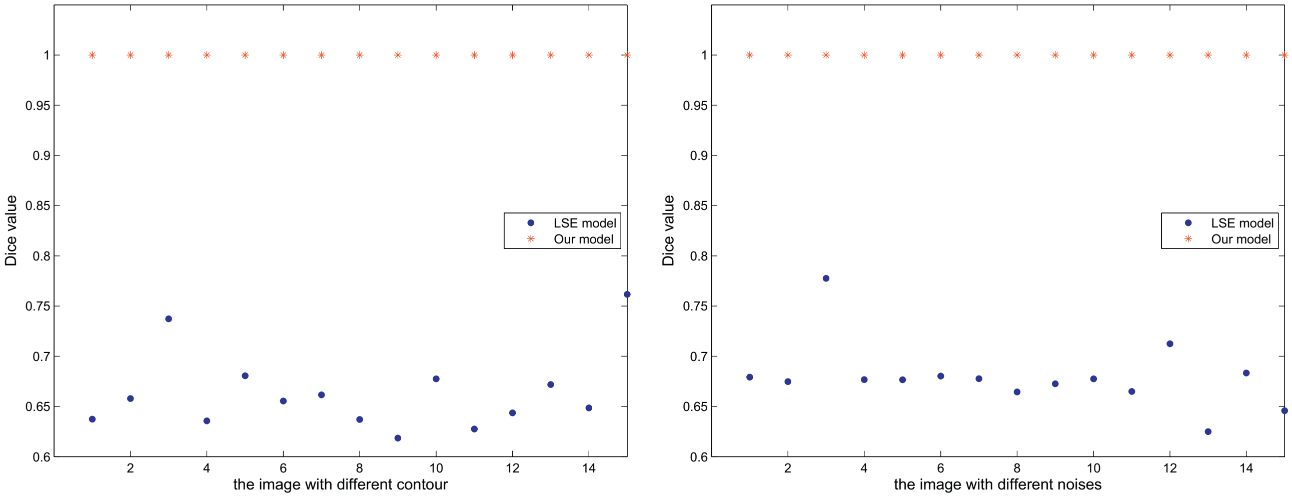

(a) (b)

Fig. 5. Dice values of the segmentation results given by the LSE model and our model. (a): Dice values with different initial contours; (b): Dice values with different noises.

the LSE model are 0.7716, 0.6339 and 0.7964, respectively, and those of the MICO model are 0.8266, 0.7792 and 0.8879, respectively. Numerical comparison verifies that the Dice values of our model are not only higher than those of the LSE model, but also obviously greater than those of the MICO model. As a consequence, numerical results quantitatively demonstrate that our model is superior to the LSE model and the MICO model in terms of the segmentation accuracy.

In addition to the Dice values, we also calculate the CV values of the LSE model, the MICO model and our model to quantitatively compare their correction effect. In Fig. 11, we show the box plots of the CV

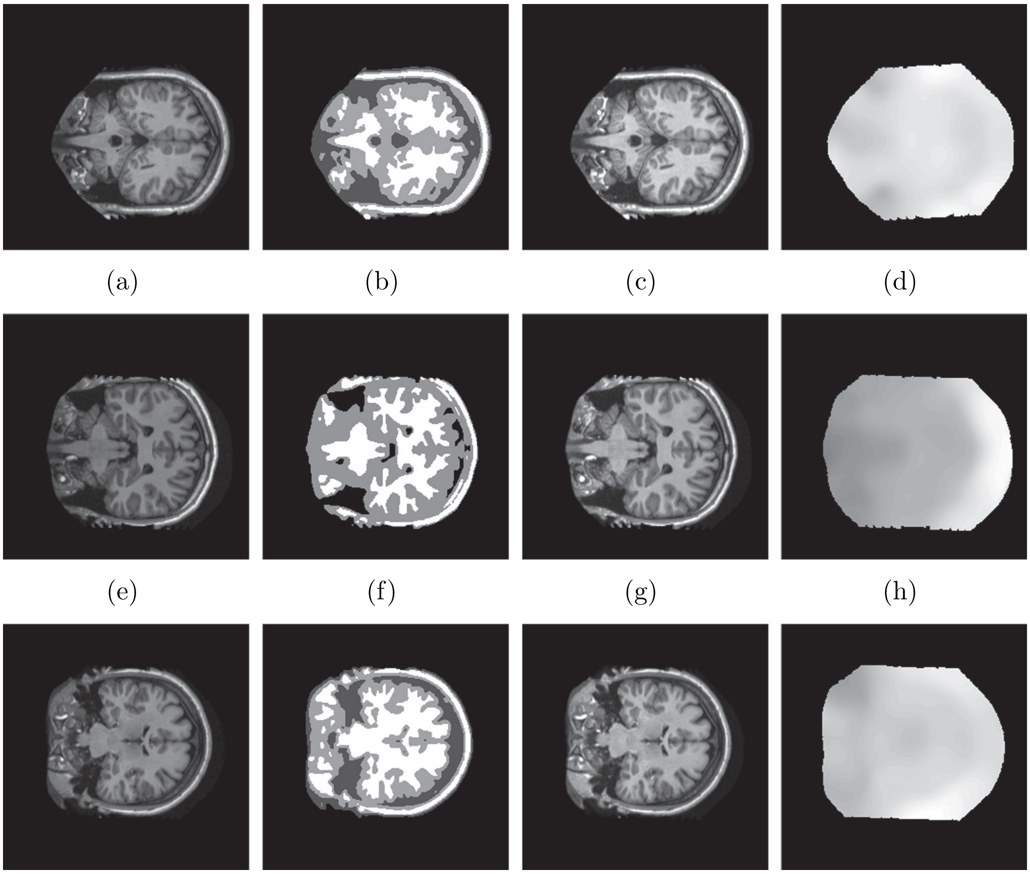

(a) (b) (c) (d)

(e) (f) (g) (h)

(i) (j) (k) (l)

Fig. 6. Application of our model to three real brain MR images. Column 1: Original images; Column 2: Manual segmentation results; Column 3: Bias correction images; Column 4: Estimated bias fields. $\sigma = 10$, $\lambda = 1$, $\epsilon = 0.01$, $\beta = 0.1$, $\lambda_1 = \lambda_2 = \lambda_3 = \lambda_4 = 1 \times 10^{-3}$.

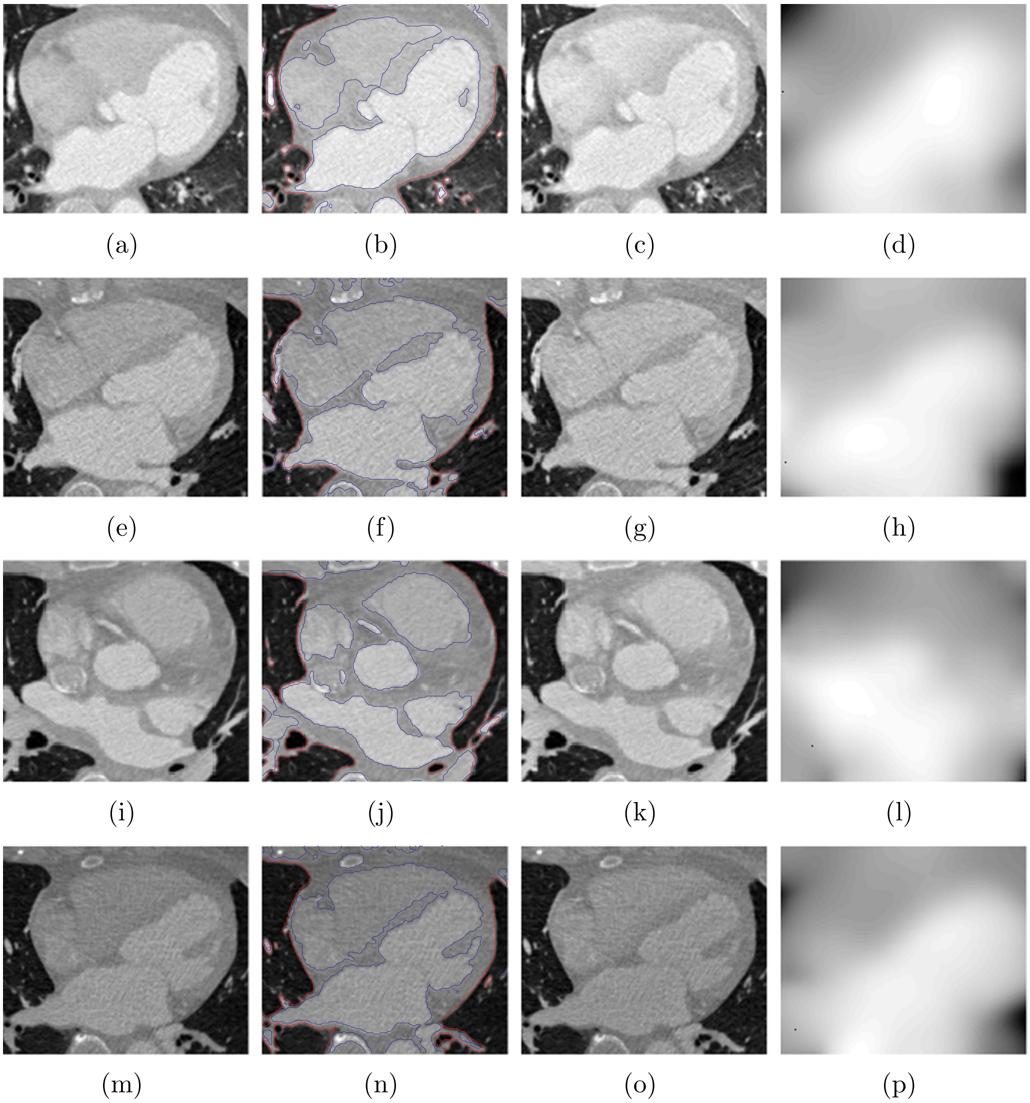

Fig. 7. Application of our model to four real heart MR images. Column 1: Original images; Column 2: Segmentation results; Column 3: Bias correction images; Column 4: Estimated bias fields. $\sigma = 12$, $\lambda = 1$, $\epsilon = 0.03$, $\beta = 1$, $\lambda_1 = \lambda_2 = \lambda_3 = \lambda_4 = 1 \times 10^{-3}$.

values for WM and GM, respectively. From the box plots of the CV values, we can visually see that the CV values of our model are not only lower than those of the LSE model, but also lower than those of the MICO model. To make the contrast more obvious, we give the specific numerical results to powerfully compare the correction effect of the LSE model, the MICO model and our model. For WM, the median, the lower quartile and the upper quartile of the CV values for our model are 0.1524, 0.1350 and 0.1695, respectively, while those of the LSE model are 0.2322, 0.2004 and 0.2659, and those of the MICO model are 0.1847, 0.1774 and 0.2003, respectively. Similarly, for GM, the median, the lower quartile and the upper quartile of the CV values for our model are 0.1377, 0.1294 and 0.1620, respectively, while those of the LSE model are 0.1692, 0.1552 and 0.2151, and those of the MICO model are 0.1573, 0.1461 and 0.1949, respectively. Through comparing specific values, we can get the same conclusion that the CV values of our model are lower than those of the LSE model and the MICO model. Therefore, comparison of the CV values quantitatively demonstrates that our model outperforms the LSE model and the MICO model in terms of correction.

4.3. Experimental results for color images

Due to the light illumination, there are very serious intensity inhomogeneities in the retina image, which poses a great challenge for segmenting blood vessels in the retina. In this section, we download the original retinal images from the Indian Diabetic Retinopathy Image Dataset (IDRID) website at https://idrid.grand-challenge.org/. Then, we cut out representative parts from three different retinal images for experimentation. We apply our proposed vector-valued model to segment three intercepted retinal images with obvious intensity inhomogeneities and show the specific results in Fig. 12. Segmentation results Column 2 tell us that blood vessels in retinal images are accurately segmented by our model. As seen from bias correction images in Column 3, our model succeeds in eliminating the effects of the bias field by decreasing the intensity of the brighter area or increasing the intensity of the darker area to make the corrected images more homogeneous and clearer than original images. All experimental results illustrate that our model has satisfactory segmentation and correction results for color images with intensity inhomogeneities.

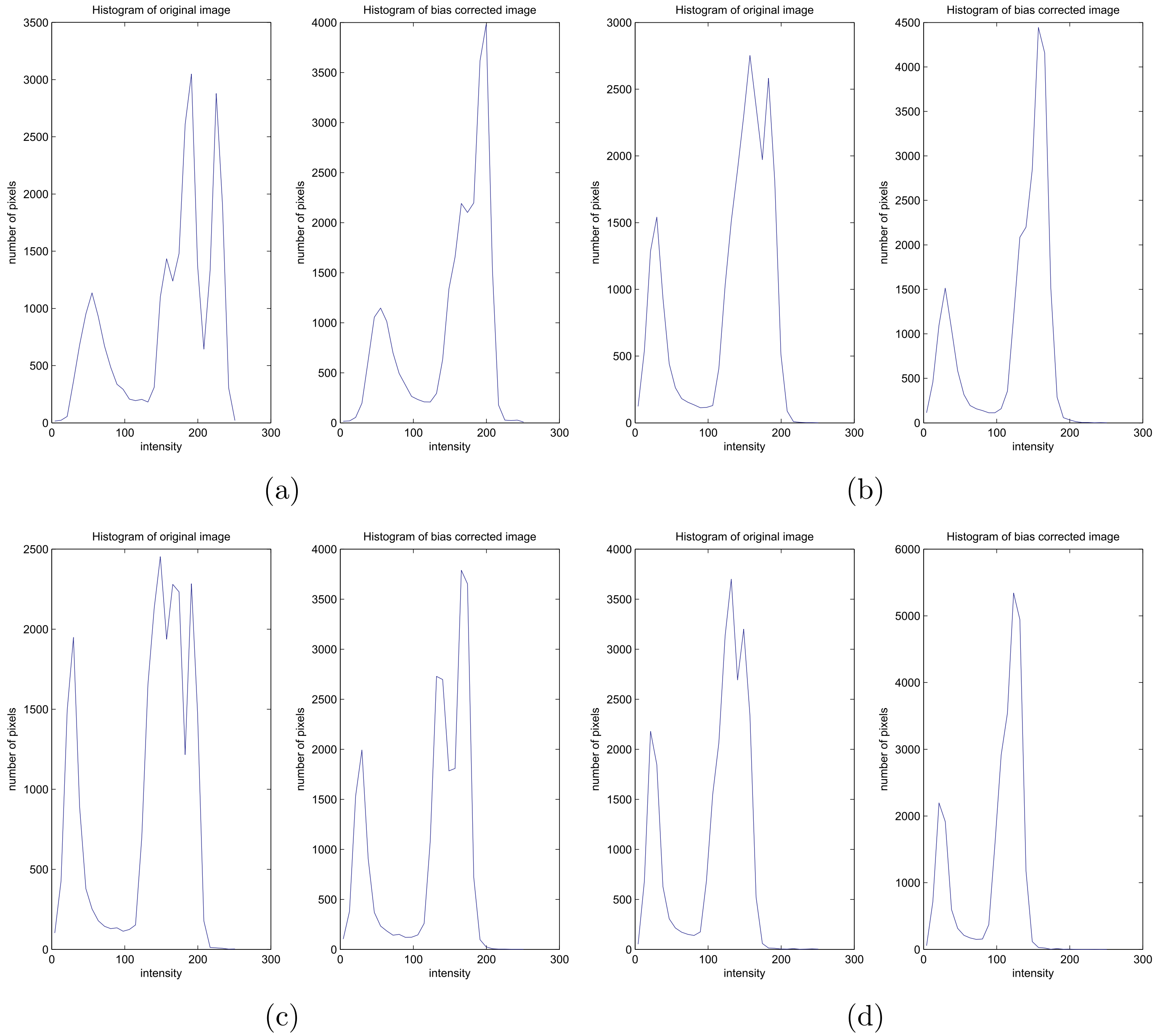

(a) (b)

(c) (d)

Fig. 8. Histogram of intensity distribution of the original image and the correction image. In each subfigure (a)–(d): The left graph is the intensity distribution of the original image, and the right graph is that of the bias correction image.

In Fig. 13, three melanoma images are used to test our model, which are downloaded from ISIC 2017: Skin Lesion Analysis Towards Melanoma Detection at https://idrid.grand-challenge.org/. From original images in Column 1, we observe that three images have different degrees of intensity inhomogeneity, and edges of the melanomas are very blurred. In this circumstance, we apply our model to segment such melanoma images. Segmentation and correction results are shown in Column 2 and Column 3, respectively. As can be seen from segmentation results, the edge of the melanoma is well detected by our model, even if it is very unclear. More importantly, our model overcomes the difficulty of intensity inhomogeneity caused by the bias field and gives more accurate segmentation results. Besides, the factor of bias has been successfully removed by our model so that correction images are more homogeneous and clearer.

4.4. *Review on results and limitations of the proposed model*

4.4.1. *Review on results*

In this paper, we mainly use three types of images with intensity inhomogeneity to test the performance of our model, including the heart MR images, the synthetic images and the brain MR images. Meanwhile, quantitative comparison experiments are also performed for all categories to further compare the segmentation accuracy and the correction effect of our model and other models.

First, for the two-phase heart MR images, we not only calculate the variance of the correction images obtained by our model and the LSE model, but also record the CPU time taken by them, which are shown in Tables 1 and 2, respectively. Comparisons of the variance and the CPU time quantitatively demonstrate that our model is superior to the LSE

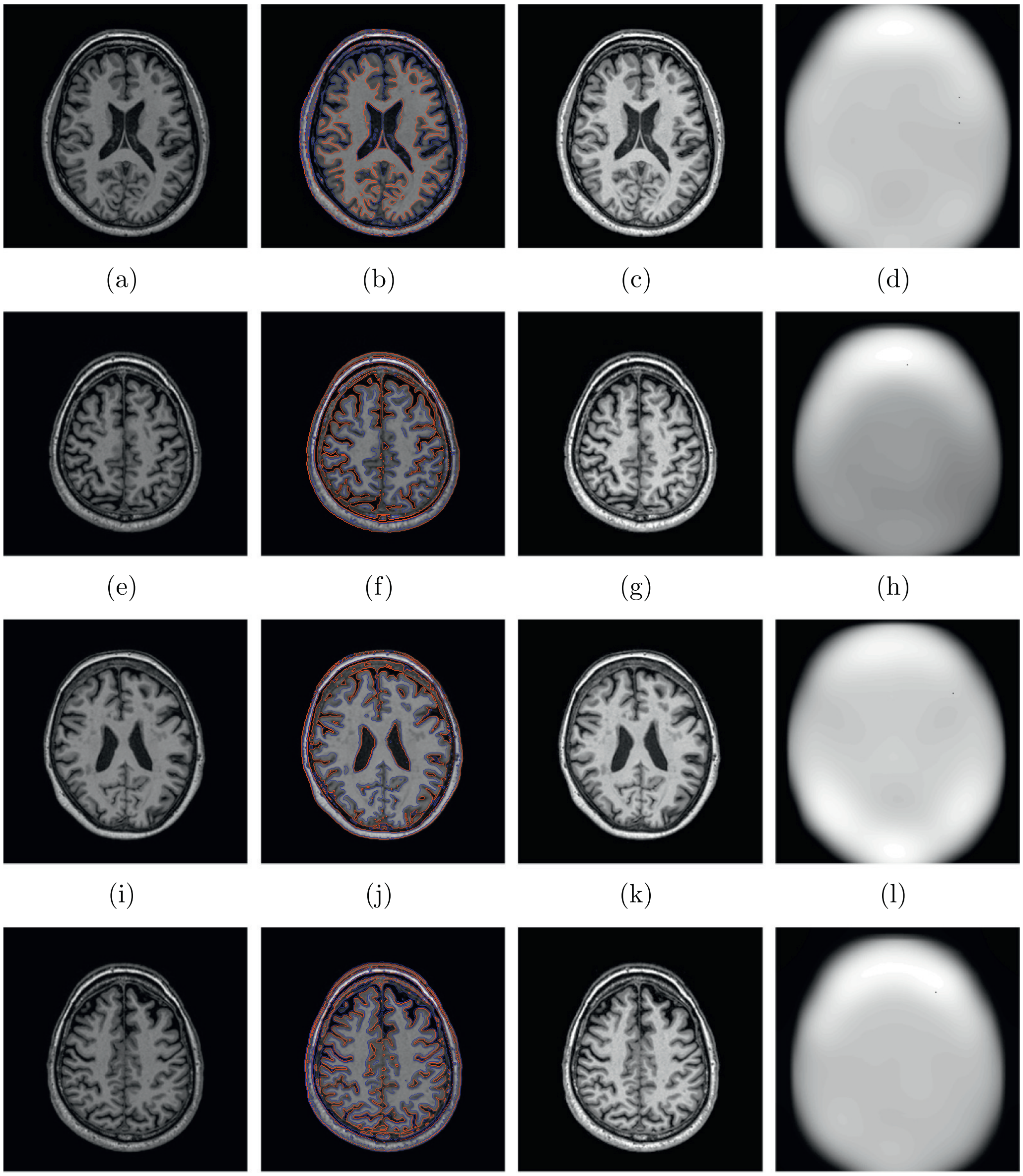

(a) (b) (c) (d)

(e) (f) (g) (h)

(i) (j) (k) (l)

(m) (n) (o) (p)

Fig. 9. Results of our model for four real brain MR images with severe intensity inhomogeneities. Column 1: Original images; Column 2: Segmentation results; Column 3: Bias correction images; Column 4: Estimated bias fields. $\sigma = 11$, $\lambda = 1$, $\epsilon = 0.08$, $\beta = 1$, $\lambda_1 = \lambda_2 = \lambda_3 = \lambda_4 = 1 \times 10^{-3}$.

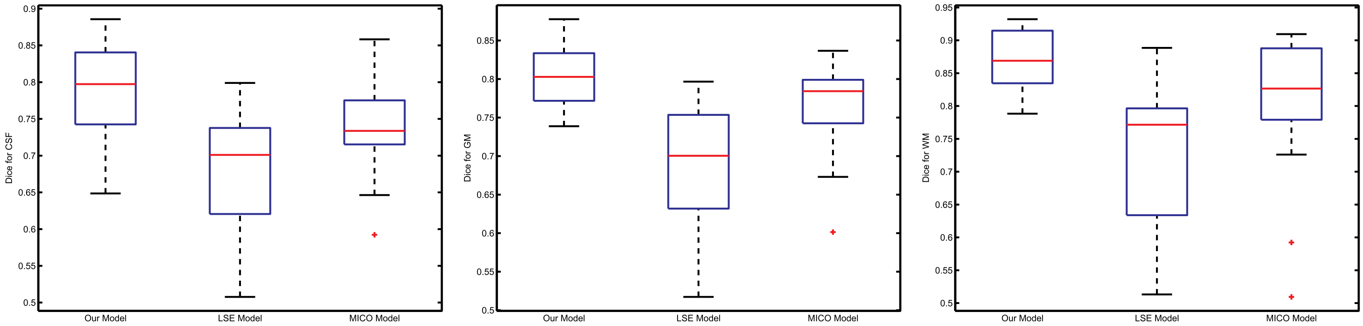

(a) (b) (c)

Fig. 10. Dice values of the white matter, the gray matter and the cerebrospinal fluid in brain MR images with the LSE model and our model. (a): The cerebrospinal fluid; (b): The gray matter; (c): The white matter.

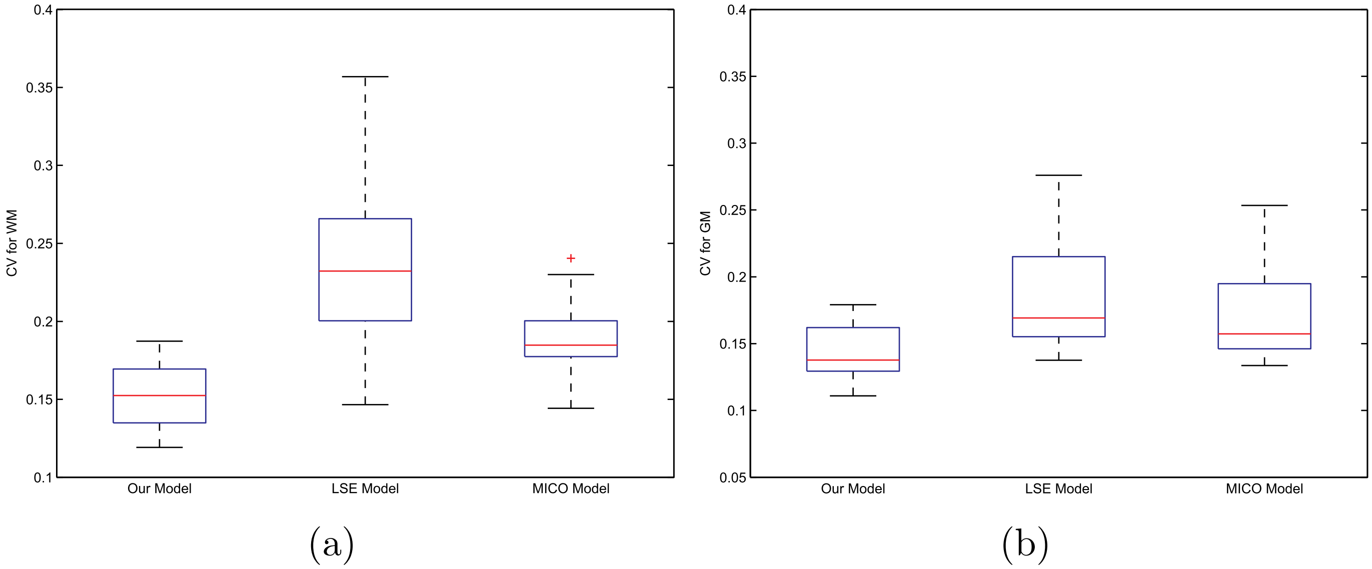

Fig. 11. CV values of the white matter and the gray matter in the bias correction images obtained by the LSE model, the MICO model and our model. (a): The white matter; (b): The gray matter.

model in correction and efficiency. Second, for the synthetic images, the Dice values for different initial contours and different noises are calculated, and are drawn as the scatter plots in Fig. 5, which quantitatively verifies that our model is more accurate than the LSE model. Moreover, the Dice values also demonstrate that our model is not sensitive to initial contours, and is robust to noises. Third, for the multiphase heart MR images, we compare the intensity distribution histogram of the original image and the correction image obtained by our model, which illustrates that the correction image is more homogeneous than the original image such that the correction effect of our model is satisfactory. Finally, for the brain MR images, we calculate the Dice values and the CV values of the LSE model, the MICO model and our model, which are drawn as the box plots in Figs. 10 and 11, respectively. Comparisons of the Dice values and the CV values quantitatively illustrate that our model is superior to the LSE model and the MICO model both in the segmentation accuracy and the correction effect. In conclusion, all comparison experiments demonstrate that our model has the advantages of accuracy, excellent correction effect and high efficiency.

4.4.2. *Limitations of the proposed model*

In this paper, we verify that our model can accurately segment and

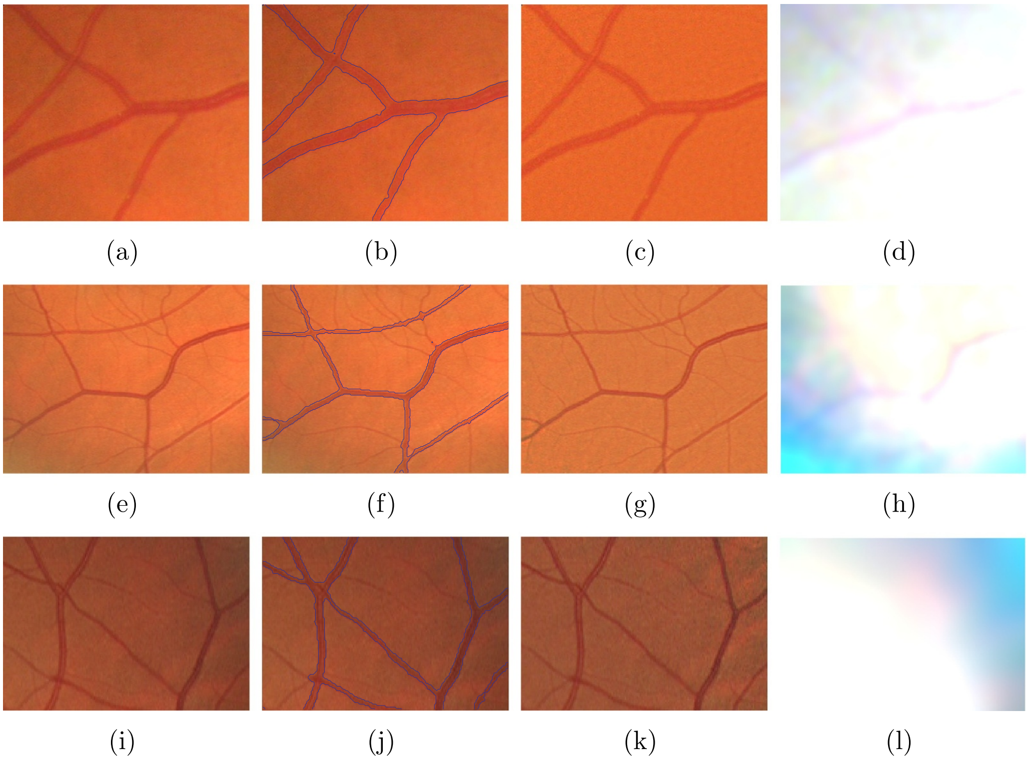

Fig. 12. Experimental results of three different retinal images with serious intensity inhomogeneities segmented by our vector-valued model. Column 1: Original images; Column 2: Segmentation results; Column 3: Bias correction results; Column 4: Bias fields. $\sigma = 10$, $\lambda = 1$, $\epsilon = 0.005$, $\lambda_1 = \lambda_2 = 1$, $\beta = 10$.

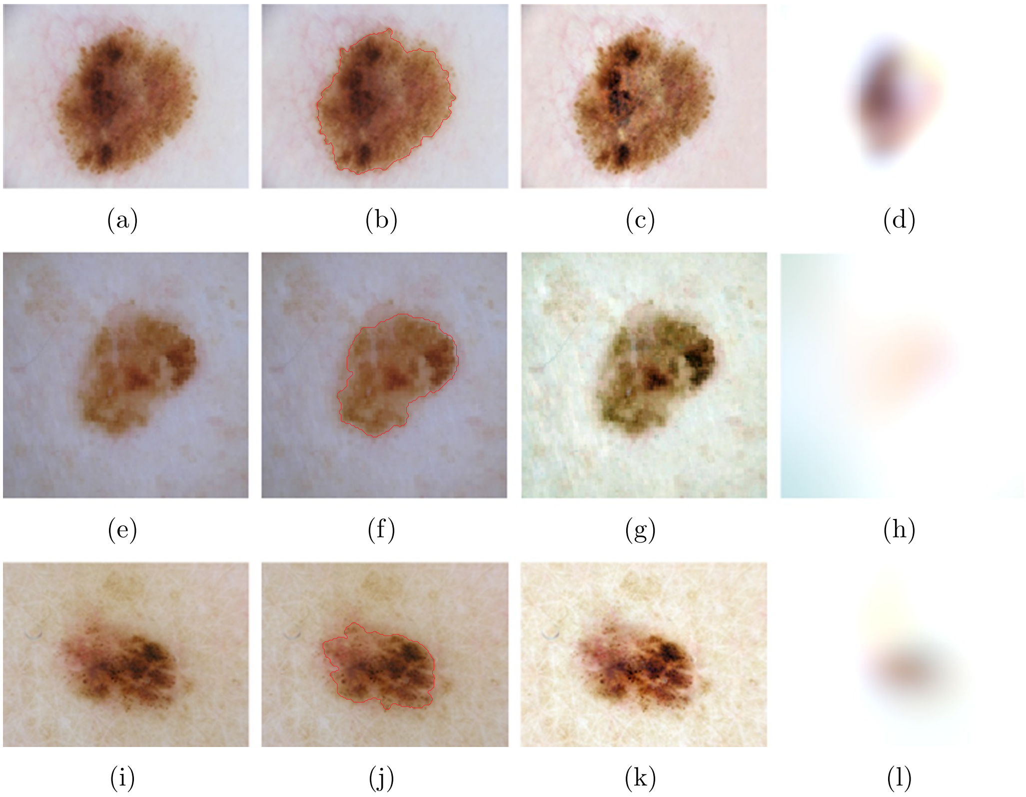
(a) (b) (c) (d)
(e) (f) (g) (h)
(i) (j) (k) (l)

Fig. 13. Segmentation and bias correction results of our vector-valued model for three different melanoma images with intensity inhomogeneity. Column 1: Original images; Column 2: Segmentation results; Column 3: Bias correction images; Column 4: Bias fields. $\sigma = 10$, $\lambda =$, $\epsilon = 0.05$, $\lambda_1 = \lambda_2 = 1$, $\beta = 1$.

correct multiple types of medical images with intensity inhomogeneity, including the two-phase, the multi-phase and color medical images. Although our model has excellent and satisfactory applications in a variety of medical images, there are still some limitations in our model. First, we have done a lot of experiments on medical images, and the experimental results have been quantitatively demonstrated to have high accuracy compared with the ground truths given by doctors, but we still lack some experiments in clinical application, and we are dedicated to this work. Second, we only apply the vector-valued model to color retinal images and melanoma images in this paper. In the future, we will collect more types of color medical images to test the practical value of the vector-valued model.

4.5. Discussion of parameters

4.5.1. Selection criteria of parameters

In all experiments, choosing the right parameters is critical to our model, and it is closely related to the accuracy of the segmentation results. There are 6 different parameters involved in our model, including σ, λ, ϵ, λ_1, λ_2 and β. In this paper, we use $\lambda = 1$ for all experiments, and use $\epsilon = 1$ for two-phase experiments. In addition, we have also listed the specific parameter values used for the images in the caption of the figure. Next, we specially explain the selection criteria and the practical significance of each parameter in our model.

The parameter σ named the scale parameter, which determines the size of the window generated by the Gaussian kernel function. In general, the size of the window is $(4\sigma + 1) \times (4\sigma + 1)$, which means the smaller the value of σ is, the smaller the window is. When σ takes a smaller value, our model will consider more local information. Conversely, a larger σ will make less local information to be considered. As a consequence, if the intensity inhomogeneity of the image is very serious, we can choose a smaller σ to accurately segment them. If the images are with slight intensity inhomogeneity, a larger σ is enough to accurately segment them.

The parameter λ is the coefficient of the quadratic penalty function in the minimization process of applying the split Bregman method, and its main function is to strictly constrain the equation $\mathbf{d} = \nabla\phi$. As we all know, one important advantage of applying split Bregman method is that we can set λ to a fixed value. In our experiment, we set $\lambda = 1$.

The parameter ϵ is used in the smooth approximation function H_ϵ of the Heaviside function H. In this paper, we choose $\epsilon = 1$ as usually.

The parameters λ_1 and λ_2 are used to balance the energy inside and outside the contour, respectively. In general, λ_1 and λ_2 take the same value. But in some special cases, we also choose different λ_1 and λ_2 to ensure more accurately fit the energy inside and outside the contour.

The parameter β is used in the edge detection function, which determines the detail level of the segmentation. When β takes a large value, even if the image gradient is very small, the edge function can accurately detect its boundary, so our model can get more contours to give more detailed segmentation results. However, if we only want to get a rough contour, we can choose a relatively small β, so that only when the image gradient is large, it can be segmented. In our experiment, we usually set $\beta = 1$.

4.5.2. Discussion on the parameter selection sensitivity

To give the optimal parameter selection, we utilize the Dice value to test the impact of different parameter combinations on segmentation accuracy. Here, we use the brain MR images in Fig. 9 to do the following experiments.

First, we discuss the optimal parameter selections for β and σ. Fixing $\lambda_1 = \lambda_2 = \lambda_3 = \lambda_4 = 1 \times 10^{-3}$, $\lambda = 1$ and $\epsilon = 0.05$, we vary the values of β with equal steps in the interval [1, 10], and vary the values of σ with equal steps in [5, 15]. Based on the above setting, we use different combinations of β and σ to calculate the Dice values for GM and WM, and record the corresponding CPU time at the same time. The specific experimental results are shown in Fig. 14. Observing Fig. 14 (a) and (c),

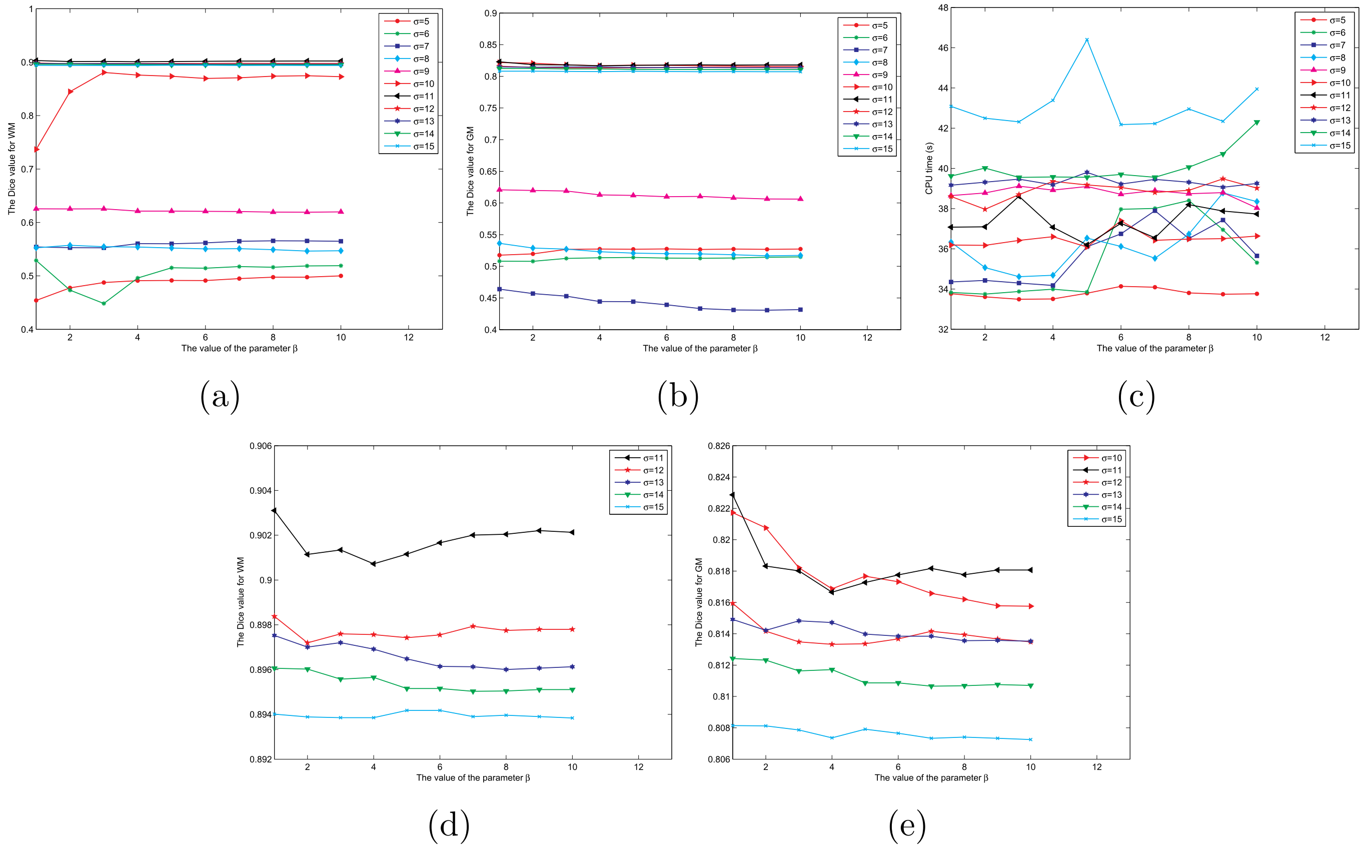

Fig. 14. The trade-off between values of σ and β versus the segmentation accuracy and CPU time.

as the value of σ increases, the Dice value and the CPU time also increase gradually. Moreover, when the value of σ reaches 11, the Dice value almost reaches a stable state, and even if σ continue to increase, the change of the Dice value is very small, but the CPU time greatly increases. Fig. 14 (d) more clearly shows the change of the Dice value with σ taking values in [11, 15]. From Fig. 14 (d), we find that when σ increases from 11 to 15, the corresponding Dice value gradually decreases. Therefore, the optimal selection for σ is 11. In addition, for the parameter β, we find with σ fixed, the change of β has little effect on the Dice value. For this reason, we can choose the parameter β flexibly. But we still can observe from Fig. 14 (d) that as the value of β increases, the Dice value is slightly reduced. To get the highest segmentation accuracy, we choose the optimal value $\beta = 1$. Besides, the situation of GM is similar to that of WM, which can be seen from Fig. 14 (b) and (e). As a consequence, we set $\sigma = 11$ and $\beta = 1$ for brain MR images in Fig. 9.

Second, we discuss the optimal selections for λ and ϵ. For the parameter λ, we vary its value with equal steps in [1, 10], while we let ϵ take values with equal steps in [0.01, 0.1]. Then, we use different combinations of λ and ϵ to calculate the Dice values and CPU time, which are shown in Fig. 15. From Fig. 15, we find when $\lambda = 1$, its Dice values are generally higher than the Dice values of λ taking other values. Besides, with $\lambda = 1$, when ϵ increases to 0.04, the Dice value is almost stable. As a result, we can choose the value of ϵ flexibly in [0.04, 0.1]. Observing Fig. 15 (c), keeping $\lambda = 1$ fixed, $\epsilon = 0.08$ spends the least CPU time. As a consequence, under the premise of obtaining higher Dice values, for the purpose of saving time, we set $\lambda = 1$ and $\epsilon = 0.08$ for brain MR images.

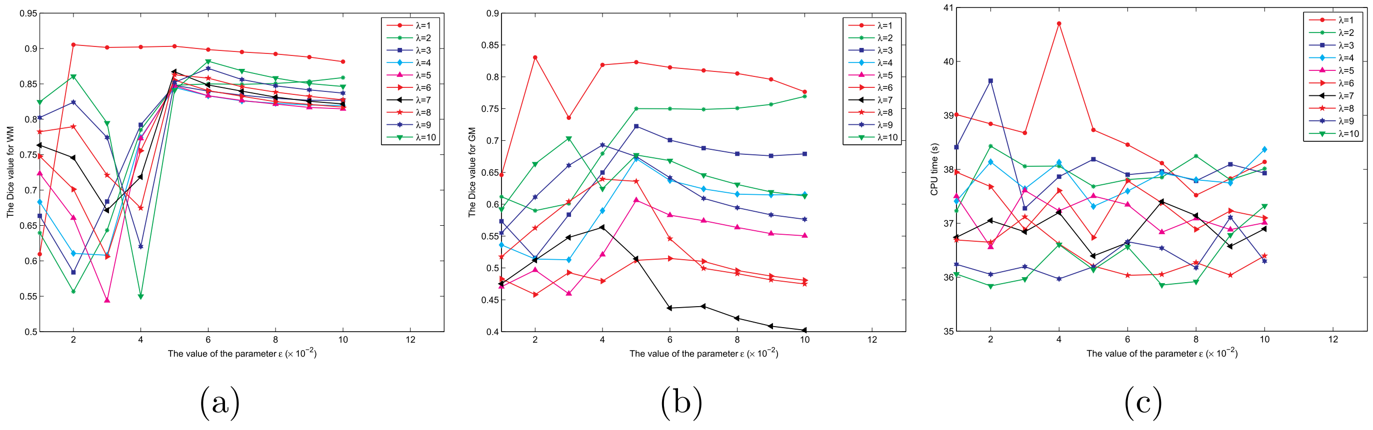

Fig. 15. The trade-off between values of λ and ϵ versus the segmentation accuracy and CPU time.

5. Conclusion

In this paper, we incorporate the bias field, the level set evolution method and the GCS method to propose an improved active contour model, including the two-phase, multi-phase and vector-valued formulations. Since the energy functionals have special structures, it's reasonable to apply the split Bregman method to minimize the proposed energy functionals. Based on our model, we can simultaneously achieve image segmentation and bias correction for images with serious intensity inhomogeneity. Large amounts of synthetic and real MR images are segmented by our model. Experimental results indicate that our model can successfully segment images with intensity inhomogeneity and give satisfactory bias correction images at the same time. Compared with the LSE model, our model not only has higher accuracy for segmentation and bias correction, but also is more efficient since split Bregman method improves the computational efficiency and reduces the iterative times. What's more important, the Dice value is also calculated to quantitatively compare our model with the LSE model, which more convincingly demonstrates that our model is superior to the LSE model. In addition, with different initial contours and noises added into images, experimental results demonstrate that our model is not sensitive to initial contour and is robust to noises. For color images, our model also provides accurate and promising segmentation and bias correction results. As a consequence, our model has a satisfactory performance for segmenting and correcting gray MR images and color images with intensity inhomogeneity.

Acknowledgments

This work is supported by Shenzhen Fundamental Research Plan (no. JCYJ20160505175141489).

References

[1] Cheriet M, Said JN, Suen CY. A recursive thresholding technique for image segmentation. IEEE Trans Image Process 1998;7(6):918–21.
[2] Wang R, Li C, Wang J, Wei X, Li Y, Zhu Y, et al. Threshold segmentation algorithm for automatic extraction of cerebral vessels from brain magnetic resonance angiography images. J Neurosci Methods 2015;241:30–6.
[3] Lopes VMG. Seeded region growing methods for automatic upwelling detection from sea surface temperature images. J Exp Biol 2015;208(11):2063–70.
[4] Chang YL, Li X. Adaptive image region-growing. IEEE Trans Image Process 1994;3(6):868–72.
[5] Chan TF, Vese LA. Active contours without edges. IEEE Trans Image Process 2001;10(2):266–77.
[6] Li C, Kao CY, Gore JC, Ding ZH. Minimization of region-scalable fitting energy for image segmentation. IEEE Trans Image Process 2008;17(10):1940–9.
[7] Wicks DA, Barker GJ, Tofts PS. Correction of intensity nonuniformity in MR images of any orientation. Magn Reson Imaging 1993;11(2):183–96.
[8] Narayana PA, Brey WW, Kulkarni MV, Sievenpiper CL. Compensation for surface coil sensitivity variation in magnetic-resonance imaging. Magn Reson Imaging 1988;6(3):271–4.
[9] Tincher M, Meyer CR, Gupta R, Williams DM. Polynomial modeling and reduction of RF body coil spatial inhomogeneity in MRI. IEEE Trans Med Imaging 1993;12(2):361–5.
[10] Condon BR, Patterson J, Wyper D, Jenkins PA, Hadley DM. Image nonuniformity in magnetic resonance imaging: its magnitude and methods for its correction. Br J Radiol 1987;60(709):83–7.
[11] Li C, Gore JC, Davatzikos C. Multiplicative intrinsic component optimization (MICO) for MRI bias field estimation and tissue segmentation. Magn Reson Imaging 2014;32(7):913–23.
[12] Ahmed MN, Yamany SM, Mohamed N, Farag AA. A modified fuzzy c-means algorithm for bias field estimation and segmentation of MRI data. IEEE Trans Med Imaging 2002;21(3):193–9.
[13] Van Leemput K, Maes F, Vandermeulen D, Suetens P. Automated model-based bias field correction of MR images of the brain. IEEE Trans Med Imaging 1999;18(10):885–96.
[14] Dawant BM, Zijdenbos AP, Margolin RA. Correction of intensity variations in mr-images for computer-aided tissue classification. IEEE Trans Med Imaging 1993;12(4):770–81.
[15] Vovk U, Pernus F, Likar B. A review of methods for correction of intensity inhomogeneity in MRI. IEEE Trans Med Imaging 2007;26(3):405–21.
[16] Li C, Huang R, Ding Z, Gatenby JC, Metaxas DN, Gore JC. A level set method for image segmentation in the presence of intensity inhomogeneities with application to MRI. IEEE Trans Image Process 2011;20(7):2007–16.
[17] Ivanovska T, Laqua R, Wang L, Schenk A, Yoon JH, Hegenscheid K, et al. An efficient level set method for simultaneous intensity inhomogeneity correction and segmentation of MR images. Comput Med Imaging Graph 2016;48:9–20.
[18] Chen YJ, Zhao B, Zhang JW, Zheng YH. Automatic segmentation for brain MR images via a convex optimized segmentation and bias field correction coupled model. Magn Reson Imaging 2014;32(7):941–55.
[19] Li C, Kao CY, Gore J, Ding Z. Implicit active contours driven by local binary fitting energy. Proceedings of IEEE Conference on Computer Vision and Pattern Recognition (CVPR). Minneapolis, MN, USA: IEEE Computer Society; 2007. p. 1–7.
[20] Kass M, Witkin A, Terzopoulos D. Snakes: active contour models. Int J Comput Vis 1988;1(4):321–31.
[21] Caselles V, Kimmel R, Sapiro G. Geodesic active contours. Int J Comput Vis 1997;22(1):61–79.
[22] Wang L, Li C, Sun Q, Xia D, Kao CY. Active contours driven by local and global intensity fitting energy with application to brain MR image segmentation. Comput Med Imaging Graph 2009;33(7):520–31.
[23] Goldstein T, Osher S. The split Bregman method for L1-regularized problems. SIAM J Imaging Sci 2009;2(2):323–43.
[24] Goldstein T, Bresson X, Osher S. Geometric applications of the split Bregman method: segmentation and surface reconstruction. J Sci Comput 2010;45(1-3):272–93.
[25] Yunyun Yang, Li Chunming, ChiuYen Kao, Stanley Osher. Split Bregman method for minimization of region-scalable fitting energy for image segmentation. International Symposium on Visual Computing (ISVC), Lecture Notes in Computer Science. vol. 6454. Berlin, Heidelberg: Springer; 2010. p. 117–28.
[26] Yang Y, Wu B. Split Bregman method for minimization of improved active contour model combining local and global information dynamically. J Math Anal Appl 2012;389(1):351–66.
[27] Yang Y, Zhao Y, Wu B. Efficient active contour model for multiphase segmentation with application to brain MR images 1355001 1–28 Int J Pattern Recognit Artif Intell 2013;27(1).
[28] Yang Y, Zhao Y, Wu B, Wang H. A fast multiphase image segmentation model for gray images. Comput Math Appl 2014;67(8):1559–81.
[29] Chan TF, Sandberg BY, Vese LA. Active contours without edges for vector-valued images. J Vis Commun Image Represent 2000;11(2):130–41.
[30] Yang Y, Wu B. A new and fast multiphase image segmentation model for color images Article ID 494761 Math Probl Eng 2012;2012.
[31] Yin W, Osher S, Goldfarb D, Darbon J. Bregman iterative algorithms for L1-minimization with applications to compressed sensing. SIAM J Imaging Sci 2008;1(1):143–68.
[32] Cai JF, Osher S, Shen Z. Split Bregman methods and frame based image restoration. Multiscale Model Simul 2009;8(2):337–69.
[33] Chan TF, Nikolova M. Algorithms for finding global minimizers of image segmentation and denoising models. SIAM J Appl Math 2006;66(5):1632–48.
[34] Vese LA, Chan TF. A multiphase level set framework for image segmentation using the Mumford and Shah model. Int J Comput Vis 2002;50(3):271–93.
[35] Yang Y, Zhao Y, Wu B. Split Bregman method for minimization of fast multiphase image segmentation model for inhomogeneous images. J Optim Theory Appl 2015;166(1):285–305.